This manuscript is a preprint and priory submitted for publication in **Tectonics**. Please note that this manuscript has not yet undergone peer-review; as such, subsequent version of this manuscript may have different content. We invite you to contact any of the authors directly to comment and give any feedbacks on the manuscripts.

Salt-detached strike-slip faulting, Outer Kwanza Basin, Offshore Angola

Aurio Erdi[1,2], Christopher A-L. Jackson[1,†]

[1]Basin Research Group (BRG), Department of Earth Science and Engineering, Imperial College, Prince Consort Road, London, SW7 2BP, UK

[2] National Research and Innovation Agency (BRIN), Indonesia

[†]Present address: Basin Studies Group, Department of Earth, Atmospheric and Environmental Sciences, University of Manchester, Oxford Road, Manchester, M13 9PL, UK

Corresponding author: Aurio Erdi (a.erdi18@imperial.ac.uk)

Key Points:

- Strike-slip faults grew in the Outer Kwanza Basin to accommodate along margin variations in the rate and magnitude of salt-detached overburden translation
- The faults nucleated as isolated segments during the Early Cretaceous, propagating and linking during the subsequent c. 77 Myr
- Displacement-distance scaling relationships display significant scatter, likely reflecting kinematic interactions between faults within the array

Abstract

We here use a 3D seismic reflection dataset from Outer Kwanza Basin, offshore Angola to examine the structure and growth of salt-detached strike-slip faults. The faults occur in four, up to 13.8 km-long, NE-trending arrays that are physically linked by restraining bend and releasing stepovers, and which presently overlie Aptian salt and base-salt relief related to pre-salt faulting. We suggest that these faults formed to accommodate along-margin variations in the rate and magnitude of differential seaward translation and salt diapirism, which commenced in the Early Cretaceous. We illustrate that the arrays grew by tip propagation of isolated fault segments, some of which linked during the Albian-Cenomanian (i.e., 113-100.5 Ma, or the initial 11-13% of their deformation history). Some arrays then reached their near-final length within the subsequent ca. 77 Ma, or the next 69-81% of their deformation history), while others attained this later, during the subsequent ca. 18 Ma (i.e., after 95% of their deformation history). During this time, the segments formed and then breached releasing and restraining stepovers, with the arrays as a whole growing by alternating periods of lengthening, throw accumulation, and inactivity. Our results also show that scatter in the D-L scaling of strike-slip faults reflect the propagation, interaction, and linkage of individual segments.

Plain Language Summary

Strike-slip faulting is a key way in which the Earth's crustal deforms, occurring when two pieces of rock or sediment slide past each other. Strike-slip faults can be very big, defining the margins of the Earth's tectonic plates, or can be relatively small, forming at the edges of landslides. Despite being widespread, the lack of natural geological examples exposed at the Earth's surface or imaged within the Earth means we have a poor understanding of the three-dimensional shape of strike-slip faults or how they grow over millions of years. In this study we use (seismic reflection) images of the rocks below the seabed offshore Angola, West Africa to reveal the geometry and deformation history of relatively large (i.e., kilometre-scale) strike-slip faults formed due to the sliding of sediments on salt, a rock weak enough to behave like a fluid over millions of years. It is likely these faults formed because sediments slid towards the Atlantic Ocean by different amounts. We show that these faults form due to the lateral and vertical linkage of smaller faults over several tens of millions of years. .

1. Introduction

Strike-slip faults are a prominent mode of crustal deformation, typically forming to accommodate differential movement between horizontally translating rock masses (Bates and Jackson, 1997; Christie-Blick and Biddle, 1985; Sylvester, 1988). Strike-slip faults are widespread on Earth, occurring in a range of settings and being of widely varying scales (Mann, et al., 2007). For example, very large thick-skinned (i.e. basement-involved) strike-slip faults can form at and define plate boundaries (Sylvester, 1988; Cunningham and Mann, 2007), whereas relatively small, thin-skinned (i.e. basement-decoupled) strike-slip faults can define the margins of submarine landslides (e.g. Bull et al., 2009), or blocks of material sliding on shale- (e.g. Escalona and Mann, 2006; Leduc et al, 2012) or salt-rich (e.g. Cartwright et al, 2012; Fernandez et al, 2020) detachments (Fig. 1a-d). In all of these settings, the faults are characterized by complex alternations between reverse- and normal-throws, with geometrically or kinematically defined segments marked by relatively sharp changes in fault strike that define restraining or releasing bends or stepovers (e.g. Christie-Blick and Biddle, 1985; Cunningham and Mann, 2007). Although numerous studies have focused on the geometry and kinematics of the strike-slip faults arrays, most are limited in that they: (i) only provide a two- (i.e. in map and/or profile view) rather than three-dimensional assessment; and (ii) do not integrate growth strata and analysis of sequential piercing points to determine fault kinematics. Exceptions to this are the field-based studies such as those presented by Peacock (1991), Kim et al. (2000 and 2001), Nixon et al (2011) and Nicol et al. (2017), and the 3D-seismic reflection data-based studies of Benesh et al. (2014), Omosanya et al. (2017), and Deng et al. (2019). Thus, in stark contrast to normal (e.g. Walsh and Watterson, 1988; Dawers et al., 1993; Cartwright et al., 1995; Walsh et al., 2002; Childs et al., 2017; Rotevatn, 2019) and even reverse (e.g. Higgins et al., 2009; Bergen and Shaw, 2010) faults, which have been extensively studied, we have a relatively poor understanding of the four-dimensional structure and growth of strike-slip fault arrays.

Salt basins represents an ideal location in which to study strike-slip fault arrays. In these locations, thin-skinned (i.e. salt-detached) strike-slip faults may form in the salt overburden to accommodate: (1) regional variability in the rate and direction of salt and overburden flow (e.g. Rowan et al, 1999; Fort and Brun, 2012) (Fig. 1a, c); and/or (2) local differential extensional or contractional strains in the overburden (Fig. 1b) (e.g. Duval et al., 1992; Cartwright et al., 2012). Physical models have specifically shown that spatial changes in salt thickness related to base-salt relief influence this differential flow and resultant strains, and thus control fault segment nucleation, growth, and linkage (Fig. 1e, f) (Dooley and Schreurs, 2012; Dooley et al, 2017). Despite providing an improved understanding of the geometry and kinematics of salt-detached strike-slip fault arrays, which may provide insights into arrays formed or forming in other settings, physical model predictions need testing with observations from natural systems.

This study represents a first attempt to document the three-dimensional geometry and kinematics of a salt-detached strike-slip fault array. To do this we use high-quality 3D seismic reflection data from the Outer Kwanza Basin, offshore Angola. These data allow us to constrain the geometry of constituent fault segments and systems, showing the arrays grew to accommodate the differential seaward translation rate of salt and its overburden, as well as salt diapirism. We also show the faults are variably linked and have boundaries defined by restraining bends and releasing stepovers. We also assess isopach (i.e. thickness) maps and throw patterns, and undertake throw backstripping to reconstruct the evolution of the array. Using these data, we assess the growth trajectory of faults within displacement-distance (D-L) scaling space, highlighting the key roles throw accumulation, lateral propagation and linkage play in controlling fault array development, in a manner similar to that documented for normal and reverse faults.

2. Geological Setting

Our study area is located in the Outer Kwanza Basin, a sub-basin of the salt-bearing passive margin of the Kwanza Basin, offshore Angola (e.g. Hudec and Jackson, 2002; 2004) (Fig. 2). The Outer Kwanza Basin stretches between the basement high of the Flamingo Platform in the east and the Angola Abyssal Plain in the west. The basin is bounded to the south by several volcanic seamounts that separate it from Benguela Basin, whereas to the north it passes into the Lower Congo Basin.

Rifting of the Kwanza Basin initiated during the Early Cretaceous, associated with the opening of the South Atlantic Ocean. Rifting occurred in response to NE-oriented extension (e.g. Maurin and Guiraud, 1993; Guiraud et al, 2010), which was partly accommodated by the formation of NE-trending transform faults (Fig. 2a) (Guiraud et al., 2010). In the Outer Kwanza Basin, these transform faults bound arrays of rift-related, NW-trending, horst-and-graben structures (Fig. 2b) (Erdi and Jackson, 2021). During the latter stage of rifting, a thick layer (up to 4 km) Aptian salt unit was deposited. This salt layer thicken seaward (i.e. westward) and along-strike (i.e. southward) (von Nicolai, 2011; Evans and Jackson, 2019), draping relief associated with the underlying rift-related structures (Fig. 2b) (e.g. Hudec and Jackson, 2004; Erdi and Jackson, 2021).

Since the deposition of Aptian salt, salt tectonics has strongly influenced the tectono-stratigraphic development of the Outer Kwanza Basin, principally through thin-skinned, gravity-driven deformation (e.g. Duval et al., 1992; Lundin, 1992; Marton et al., 2000). The gravity-driven deformation is expressed as kinematically-linked zones of updip extension above the Flamingo Platform, and downdip contractional toward the seaward edge of the salt (Fig. 2a) (Hudec and Jackson, 2004). These two zones are connected by an intermediate zone of translation that has undergone multiple phases of extension and contraction due to salt and overburden flow over prominent base-salt relief (Evan and Jackson, 2019; Erdi and Jackson, 2021). Overall, the overburden has translated seaward up to 23 km (Jackson and Hudec, 2005), with local rotations of up to c. 32^{o} (Evan and Jackson, 2021) and salt-detached strike-slip faulting (i.e. tear fault; Lundin, 1992 or transfer fault; Duval et al, 1992) accommodating the variable rate and magnitude of the seaward flux of salt and its overburden. Critically, the horizontal translation of salt and its overburden mean that overburden structures (including the strike-slip fault arrays) are unlikely to be the same position as where they formed, nor do they directly overlie the base-salt features that triggered their initial development (see Erdi and Jackson, 2021).

A recent study illustrates that although overburden strike-slip faults have similar strikes and are locally physically-linked with the NE-trending, basement-involved transform fault, they are of different ages and are kinematically separate systems, i.e., the overburden strike-slip faults are post- (rather than pre-) Aptian and formed to accommodate along-strike differences in salt-related contraction and/or extension, (rather than basement-involved, subsalt blocks) (Fig. 2b) (Erdi and Jackson, 2021). In this study, we focus on the three-dimensional geometry and kinematic analysis of four large strike-slip faults within the broader array.

3. Dataset and Methods

3.1. Dataset

We use a post-stack depth-migrated BroadSeis™ 3D seismic reflection dataset that covers c. 714 km^2 of Outer Kwanza Basin, Offshore Angola (Fig. 2a). This dataset images down to the base of the Aptian salt (c. -5.5 km), with an estimated spatial resolution of c. 3.5 (λ=14 m) at the seabed and c. 30 m (λ=120 m) at a depth of 5 km. The dataset has a record length of 10 s (although the image is truncated at base-salt), a vertical sampling rate of 2 ms, and a line spacing of 25 m, with inlines and crosslines being oriented normal and perpendicular, respectively, to the broadly southwestward-directed, tectonic transport (i.e. translation) direction. The data are displayed with the SEG 'reverse' convention, where a downward increase and a decrease in acoustic impedance are represented by negative (white) and positive (black) reflection events, respectively.

3.2 Stratigraphy and structural framework

We map eight seismic horizons (i.e. base-salt, Aptian salt, Albian, Eocene, Oligocene, Lower Miocene, Upper Miocene, and seabed) across the study area using the seismic-stratigraphic framework of Erdi and Jackson (2021). These horizons are used to generate structure maps that allowed us to determine the three-dimensional geometry of the base-salt surface, and overlying salt and overburden structures, including the salt-detached strike-slip fault array (see section 3.3; Fig. 3). We overlay structure maps to show *present* distribution and relationship between base-salt, salt structures, and the strike-slip faults (Fig. 4c) (c.f. Pichel et al., 2019 and Erdi and Jackson, 2021). We also generate salt and overburden isopach maps, which reveal the present structure of the salt layer and thickness variations related to and timing of overburden deformation, respectively (Fig. 4a, b). Finally, we generate variance maps (e.g. Bahorich and Farmer, 1995) along specific seismic horizons to map faults and piercing points (e.g. channels) (Figs 5 and 6).

3.3 Analysis of fault geometry and kinematics

We use the following five techniques to document the three-dimensional geometry of salt-detached, strike-slip faults above base-salt reliefs and to constrain their kinematics: 1) displacement-distances analysis (Tx) (Fig. 3a-c); 2) displacement backstripping (e.g. Rowan et al., 1998; Dutton and Trudgill, 2009; Jackson et al., 2017); 3) fault growth trajectory plotting (see Rotevatn et al., 2019 and Pan., et al., 2022); 4) throw-depth analysis (Tz; e.g. Mansfield and Cartwright, 1996; Cartwright et al., 1998; Tvedt et al., 2016; Jackson and Rotevatn, 2013) (Fig. 3d-e); 5) expansion indices analysis (EI) (e.g. Thorsen, 1963; Jackson and Rotevatn, 2013; Reeve et al., 2015; Tvedt et al., 2016) (Fig. 3f); and, 6) isopach map analysis (e.g. Jackson and Rotevatn, 2013; Tvedt et al, 2013) (Fig. 7) (see Appendix A for full details of these various methods). Our determination of Tx (i.e., the point of maximum throw on the fault) is defined by constraining their lateral offset and throw. The lateral offset is defined by measuring the *horizontal* offset of piercing points across structures (i.e., salt structures, faults, and channels) (e.g., Peacock, 1991; Kim et al., 2001), whereas the throw is defined by measuring, in two-dimensional cross-sectional view, the *vertical* displacement of stratigraphic horizons (e.g., Omosanya et al., 2017; Deng et al., 2019).

4. Structural Framework

4.1 Base-salt

The stratigraphic surface defining the base of the salt (base-salt) broadly dips to the southwest and is characterized by three distinct trends of relatively steeply dipping (>10^{o}) areas called 'ramps' (Fig. 4a). The first trend is defined by NW-trending ramps that are up to c. 13 km long and which, in the northeast of the study area, define the southwestward edge of the Flamingo Platform (see Fig 2a). The second trend is represented by N-trending ramps that are up to c. 10 km long, and which occur in the central and south-eastern parts of the study area. Between these first two trends we observed three sub-triangular, local structural highs, which have relief of up to c. 10 km (U, V, W; Fig. 4a). The long axes of these structural highs trend broadly NW-to-N, and they dip either basinward (i.e. to the SW) or landward (i.e. to the NE). The N-trending ramps and associated local structural highs may be relicts of the Angola-Gabon horst-block systems that formed during Early Cretaceous rifting (e.g. Hudec and Jackson, 2004; Erdi and Jackson, 2021). The third set of base-salt ramps trend NE and thus intersect the NW-trending ramps. They are up to c. 6 km long and dip either NW or SE and (Fig. 4a). These ramps are parallel to basement-involved transfer fault zones (e.g., the Martin Vaz Fault Zone in Fig 2a; Moulin et al., 2005; Guiraud et al., 2010) and may thus be the upper crustal expression of these lithosphere-scale structures (Erdi and Jackson, 2021).

4.2 Salt structures

The salt isopach map shows that Aptian salt has flowed to form a suite of salt structures (e.g., anticlines, walls) that are locally separated by apparent primary salt welds (Fig. 4b, c) (*sensu* Wagner and Jackson, 2011). Secondary welds separate minibasins adjacent to squeezed diapirs

(SN and SQ; Fig. 9). Salt anticlines (SA and SN) are >0.5 km wide, >1.3 km long, and have relief up to 0.7 km height, whereas salt walls (SW and SQ) are far larger, being >1.1 km wide, up to 47 km long, and having relief of up to 3 km height (Fig. 9), extending from the Aptian source layer up to the seabed (i.e. SW2; Erdi and Jackson, 2021).

4.3 Supra-salt structural styles

The distribution and style of supra-salt structures vary across the study area and are best-illustrated with the variance attribute maps (Fig. 5). These maps show that normal, thrust, and salt-detached strike-slip faults are common, with these structures being at least c. 2 km, 5 km, and 5 km long, respectively. These faults have variable trends and spatial relationships, lying parallel, perpendicular, or oblique to one another and adjacent salt structures (Fig. 5). Erdi and Jackson (2021) explore the geometry and timing of growth of the various salt structures and related normal and thrust faults, and how these relate to the geometry of the base salt surface. We here now focus on the strike-slip fault array.

5. Geometry of Salt-detached Strike-slip Faults

5.1 Overall structure

We observe five, NE-to-NNE-striking, salt-detached strike-slip fault systems that show increasingly complex geometries upwards within the cover strata (F1-5; Figs 4b and 5). They are broadly characterised by a long (up to 13 km), approximately linear fault traces, that terminate against normal faults, die-out into salt structures, or simply terminate within the overburden. The trace length of F4 (i.e. F4a, b) increases upwards, but decreases upward for F1-F3. At the top Albian, F3-F4a have long, linear fault traces (Figs 5a and 6b), whereas F1-F2 comprise a main structure (F1a and F2a) and an antithetic array (F1b and F2b) that are physically-linked; in these latter cases, these zones of linkage are defined by asymmetrical, graben-like structural lows (i.e. negative flower structures; e.g. Harding, 1985; Sylvester, 1988; Leduc et al., 2012), reflecting extensional stepover (Figs 5a, 6a, 10b-f). Shallower in the stratigraphy, at the top Eocene, although the long, linear fault traces still exist, many faults are characterized by several short (up to 5 km long) segments, giving rise to an overall *en echelon* pattern. Individual segments are hard- or soft-linked (F1-F4a; Figs 5b) (sensu Peacock & Sanderson, 1994; 1995). For example, segments defining F3 traces are physically linked, whereas those associated with F2 are physically unlinked and separated by a relay zone (Fig. 6c-d). At this structural level, we also observe a normal fault-dominated splay zone between F1 and the F2, and at the northeastern lateral tip of F4a (Figs 5b and 6c-d). Only F1a and F4a and F4b and their antithetic array (F1b and F4c) extend up to the structural level of the top Miocene, where they are defined by relatively continuous traces, and separated by an extensional stepover (Figs 5c and 6e-f).

In addition to displaying vertical changes in map-view geometry, salt-detached strike-slip faults vary in terms of their cross-sectional geometry and vertical extent (Fig. 10). The faults are moderate-to-steep dipping (45^{o}- 80^{o}) and are generally characterized by normal and/or reverse throws of up to 830 m. In cross-section, it is also clear that the faults decrease in height seaward, dying-out upward into progressive older stratigraphy. For example, in the NE they tip-out into intra-Oligocene strata, whereas in the SW they tip-out into Miocene strata or extend to the present seabed (Figs 5-6 and cf. Fig. 10a-d and e-g).

We observe many unequivocal piercing points along strike of the strike-slip faults and at various structural levels (e.g. salt anticlines and walls, normal and thrust faults, and channels). These points define sinistral lateral offsets of up to 1.6 km (Figs 4-6). First, at the top salt, the faults offset presumably older (i.e. pre-existing) salt structures (SQ1, SQ2a-b, SN1a-b, SA2-5; Fig. 4b). Second, at shallower structural levels, within top Albian-to-Miocene overburden, the faults offset normal and thrust faults (Figs 5 and 6). Finally, at the top Miocene, several deep-water channels represent piercing points (CH1a-e; Figs 5c and 6e-f). Strike-slip faults thus divide the salt and overburden into six sub-domains that are principally characterised by differing styles and magnitudes of salt-related deformations (Figs 5, 9 and Table 1).

Having described the two-dimensional geometry of the salt-detached strike-slip faults, we now describe and interpret the three-dimensional geometry and kinematics of the four largest and best-imaged faults.

5.2 Along-strike variations in lateral offset and throw

We use various salt- and channel-related piercing points at top salt and Albian-to-Miocene to determine along-strike changes in lateral offset along the strike-slip faults (Figs 4b, 5-6), showing this varies from 100-1683 m (purple dotted line in Fig. 8a, c, e, g). Offset vs. distance plots are generally characterized by up to four fault arrays (labelled 1-4; Fig. 8). Each array is defined by either the symmetric or asymmetric distribution of offset, defined by either a flat-topped profile, such as second array in F3a, or a peaked profile, such as second array in F1a. In general, however, maximum lateral offset occurs near the fault centres, decreasing to the lateral tips, where faults may physically link with adjacent structures. Lateral offset (strain) gradients range from 0.09-0.76, which are within the range of those reported for normal faults in the British coalfields (0.001-0.067; see Walsh and Watterson, 1988 and Nicol et al., 1996) and imaged in seismic reflection data (0.007-1.05; see Nicol et al., 1996, Jackson and Rotevatn, 2013 and Tvedt et al, 2016).

We record throw at the top of Albian, Eocene, and Upper Miocene structural levels (Fig. 8). Plotting throw against along-strike distance reveals multiple negative and positive values, which reflects normal and reverse throws, and that define a segment in the constituent array observed in map-view (see above). These segments have a maximum throw of up to 800 m and are defined at their lateral tips by throw minima. Throw gradients range from 0.10—6.3, being highest where a segment defined by normal throws passes into one defined by reverse throws, or vice versa. Throw vs. distance plots are either symmetrical and defined by a well-defined throw maxima (i.e., a peak; e.g. label 11f in Fig. 8a), or asymmetric and flat-topped (e.g. label 11f in Fig. 8b). Some plots show a gap between these various throw patterns due to the presence of salt diapirs (i.e. wall) or weld (e.g. label 11b in Fig. 8b and label 11af in Fig. 8h). Maximum throw (d_{max}) typically occurs at the top of the Albian, or more rarely at the top of the Eocene or Upper Miocene, in particular near areas of diapirism or welding (Fig. 8). To constrain how throw varies both along-strike and vertically upwards, into younger strata, we use selected inflection points on the lateral offset vs. distance plot, and distinct changes in throw at the Albian level (i-xix; Fig. 8), given this level defines the top of pre-kinematic strata and thus records most if not all of the strike-slip related strain (Erdi and Jackson, 2021).

5.3 Vertical variations in throw

Our Tz plots illustrate a more high resolutions of the throw on the various lateral distribution of the throw-distance of the strike-slip faults (Fig. 11). The plots are characterized by broadly asymmetric distribution profiles along strike. These profiles consist of up to two throw maxima, defined by either normal or reverse throws, typically located: (i) near the top of the Albian (labelled

1 in Fig. 11); (ii) the top of the Eocene or intra-Eocene (labelled 2 in Fig. 11); and, where the F1 and F4 are close to the SW2 and SW4, (iii) the top of the Lower and Upper Miocene (labelled 3 for F1 and F4 in Fig. 11). These two throw maxima are separated by a polarity reversal (i.e. normal to reverse throw, or vice versa) and a throw minima, which typically occurs in intra-Eocene strata and near the top of the Oligocene, respectively.

From the lower throw maxima downward to the top of salt, we speculate that the throw values gradually decrease, with any strain within the salt being diffuse (dotted line in Fig. 11). Upwards from the upper throw maxima, the style of throw decrease varies along strike of individual faults, depending on the structural level at and the manner in which the fault tips outs (i.e. the fault tips out within younger strata seaward and/or links with a salt wall and weld; see above). Overall, however, we observe that the throw gradients above where polarity reversals occur are high (0.23-1.92; e.g. Fig. 11c, l, u), whereas those above throw minima or toward upper tip are relatively low (0.08-to-1.42) (e.g. Fig 11g, h, ac).

5.4 Spatial and geometric relationship between strike-slip faults and base-salt relief

The salt-detached strike-slip faults vary in terms of their spatial relationship with base-salt relief. Although some parts of these faults overlie areas where the base-salt is relatively flat, such as the southwestern end of F2a, many faults strike sub-parallel to NE-trending ramps or the more elliptical base-salt highs (Figs 4c and 8). The faults also display varying degrees of physical linkage with the underlying base-salt relief, with some apparently being hard-linked (Figs 10c-f and 11). A key observation of the relationship between base-salt relief and the overlying strike-slip faults is that the maximum throw for each fault, whether located at the top of the Albian or Eocene, are *presently* and broadly underlain by the NE-trending ramps (e.g. label 10d in Fig. 8a and 11O in Fig. 8b).

5.5 Strike-slip fault-related thickness variations and their relationship with throw

We see four key thickness patterns in the overburden adjacent to array of strike-slip faults and associated structures. The first pattern is defined by several, up to 1.4 km thick and 4 km long depocenters that broadly trend perpendicular to and are intersected by, the strike-slip faults (white dotted lines in Fig. 7). These patterns include some ramp syncline basins (RSBs of Evans and

Jackson, 2021; Fig. 7d) that differ in size across the faults, and that therefore likely record different rates of overburden translation seaward. The second pattern is defined by areas of stratal thinning that are up to c. 0.3 km thick and c. 2.5 km long, and that trend broadly parallel to the strike-slip faults (green dotted lines in Fig. 7a-c, d, f). More specifically, areas overlie pop up-like structural highs, which likely reflect local contraction along a restraining bend in the fault (Fig. 8) (e.g. Cunningham and Mann, 2007). This pop up-related thinning is located where normal throw passes into vertical throw, and near an inflection point of lateral offset. The third pattern is characterised by several fault-parallel depocenters that are c. 0.6-1.4 km thick and c. up to 12 km long, that which are bound by a main strike-slip fault segment and an antithetic fault along the F2a and F4a-c (light blue dot line in Fig. 7c, g, h). This depocenter locally spans areas of normal throw on segments identified at either the Eocene or Miocene structural level (Fig. 8). We interpret this depocenter as a transtension-related, pull-apart basin developed at releasing stepovers (e.g. Sylvester, 1988; Mann, 2007). The fourth pattern is defined by several, c. 0.25-1.4 km thick and up to c. 2 km long, N-trending depocenters that are flanked by the normal fault-dominated splay zones between F1 and F2, or at the lateral tip of F4a. We interpret that these depocentres record growth of these extensional splays and thus the related strike-slip fault segments (labelled 'i' ; Fig. 7c, e, f) (e.g. Kim et al., 2004; Peacock and Sanderson, 1995).

The distribution of these types of depocenters and the thickness variations that define them record the growth of strike-slip fault array and associated structures. Albian thickness maps show that the fault-intersected depocenters and pop up-related thinning span 34-65% of the present trace lengths of F2a and F3 (Fig. 7a-b). In contrast, these types of thickness variations are only locally developed (up to 18% of the present trace length) along the F1a and F4a (Fig. 7b). Eocene-Oligocene thickness maps show that the fault-intersected depocenters and pop up-related thinning are broadly distributed along F1-F4a, indicating the related faults were growing at this time (Fig. 7c-f). However, thickness patterns in the Eocene-Oligocene strata differ to those in the underlying (i.e. older) Albian strata in two key ways: (i) distribution of the fault-intersected depocenters and pop up-related thinning decreases from up to 65% along F2a and F3 to only a maximum of 33% along F3a in the Oligocene, and; (ii) the extensional stepover depocenters that reflect activity of the splay zone. Upper Miocene-Seabed thickness map show a distinctive transtension-related depocenter that spans up to 59% and 87% of the present traces of F1 and F4a-b, respectively (Fig.

7g-h). These maps also show that Upper Miocene-Seabed strata thin towards salt walls SW2 and 4.

EI profiles provide further, quantitative insights into overburden thickness patterns both along-strike and down-dip of the strike-slip faults. We observe that EI values >1 (i.e. thickening-into-the-hangingwall) are correlate with areas of normal throw (label i; Fig. 11), whereas values <1 (thickening-into-the-footwall) correlate with areas of reverse throw (label ii; Fig. 11). EI values >1 also occur where reverse throws are observed (label iii; Fig. 11); in this case we interpret that rather than demonstrating either stratigraphic thickening or thinning into the hangingwall of a (dipping) strike-slip fault, as shown by the overburden map (Fig. 7), these values reflect the across-fault juxtaposition of differing thickness in depocentres due to strike-slip faulting.

Thickness variations associated with the fault arrays reveal that activity on these structures varied through time and space (Figs 7 and 11). The fault arrays were active since at least 100.5 Ma (Albian). Still, the F2a and F3 were active until 23 Ma (Oligocene), whereas F1a and F4a-b are likely still active.

6. Origin and evolution of strike-slip fault systems in the Outer Kwanza Basin

Having described: (i) the geometry of the strike-slip faults and their relationship with base-salt relief, and salt- and other salt-related structures in the overburden; and (ii) thickness changes in related growth strata, we now consider the origin of these structures, before reconstructing their evolution. Key to this is our ability to backstrip displacement on the faults, which thus allows us to plot fault growth trajectories (i.e., throw-distance relationships through geological time) (e.g. Chapman and Meneilly, 1991, Dutton et al., 2009; Tvedt et al., 2016).

6.1 Nucleation of the salt-detached strike-slip fault arrays and the role of base-salt relief

Erdi and Jackson (2021) argue that the Cretaceous-Neogene strike-slip fault array in the Outer Kwanza Basin are physically detached (due to the presence of Aptian salt) from the NE-trending, transform-related base-salt relief. This is consistent with our Tz analysis, showing that maximum throw on many of the strike-slip fault segments is located near the top Albian or shallower (Fig. 11). In terms of the trigger for fault nucleation, we suggest the following: (a) originally thin salt on the NE-trending base salt high flowed seaward slower than the thick salt next to the high (see variable salt flux across dip-parallel base-salt relief in the physical models of Dooley et al., 2017); and/or; (b) different seaward translation rate across the faults (Fig. 5; Erdi and Jackson, 2021). The former interpretation cannot be conclusively resolved by our study because of the *present* spatial relationship between the salt-detached strike-slip faults and base-salt relief is highly unlikely to reflect their relationship when the fault was formed, given salt and its overburden flowed seaward by at least 13 km after fault nucleation in the Albian (Fig. 4c; Erdi and Jackson, 2021). Although the former interpretation is plausible, at least the latter interpretation has been clearly demonstrated in our study area, suggesting that different seaward translation rate already occurred perpendicular to the array of strike-slip faults in Albian (i.e. the initial 11-13% of their fault histories; Fig. 12). Thus, fault nucleation likely occurred updip to the NE, outside of the presented study area (sensu Erdi and Jackson, 2021). Furthermore, the fact that the faults appeared to nucleate near the top of the Albian interval, some distance (i.e. at least 800 m) above and yet parallel to the NE-trending ramp, suggest that after forming, these faults propagated downward into and through the salt, in some places then coincidentally linking with underlying base-salt highs.

6.2 Growth of the strike-slip fault array

Having established: (i) the geometry of the strike-slip fault array; (ii) the present relationship between the faults within this array, and spatially related salt structures and base-salt features (e.g., ramps); and (iii) that the faults nucleated near the top of the Albian and are thus post-Albian, we now reconstruct the growth history of the salt-detached strike-slip faults using thickness patterns in growth strata and the fault geometries.

6.2.1 Late Albian (113-100.5 Ma)

Until at least 100.5 Ma, the constituent segments of F1a-F4a were physically isolated from one another (i, iv and xii-xix), whereas some segments had linked to form a through-going, strike-slip fault array (ii-iii and vii-x; Fig. 12 and Fig. 13a). Segment linkage was associated with the formation of restraining bends, recorded by areas of pop up-related thinning (Fig. 7, and green colour at 113-100.5 Ma; Figs 12a and 13a). As a result of these kinematics, the fault array was associated with coeval normal and reverse slip.

6.2.2 Late Cretaceous-Paleogene (100.5-23 Ma)

During the first part of this period, from the Late Cretaceous until the Eocene (from 100 to 34 Ma; i.e. capturing 69-81% of the total slip history of the faults), the constituent segments (i-xvi and xix) of F1a-F4a continued to grow by vertical and lateral propagation of their tips. Fault growth involved both dip and strike linkage (orange colour of ii-xvi and xix; Fig. 14a-d; see also at 34 Ma; Fig. 12 and BP and RL; Fig. 13b), or via tip propagation of a single structure (which may not have reached the free surface) through the overburden, similar to that documented for normal faults (e.g. Baudon and Cartwright, 2008). The interpretation that some faults never reached the free surface is supported by the constant low throw gradient (<1.00) observed near the upper tips of some segments (e.g. Fig. 11e, f), whereas the dip linkage is supported by the observation of multiple throw maxima at Eocene and near Albian structural level (Fig. 11 c, l, u, y). Some throw maxima at the Eocene structural level are defined by normal offsets (Fig. 11 l, u, y), indicating the established segments formed during the Albian dip-linked with overlying extensional faults at this time (RL on F2a; Fig. 13). Locally, however, reverse throw maxima are observed at this structural level (Fig. 11c), located near an area of pop up-related thinning in the Eocene (Figs 7c-d and label 11c; Fig. 8). These observations suggest the strike-linkage of segments was associated with restraining bend-related deformation, involving; (i) local uplift of a formerly normal fault-bounded block; and (ii) dip-linkage between deep faults with normal throw and shallower faults with reverse throws (RL on F1a; Fig. 13).

A few new segments also nucleated along F4a during this time (xvii-xviii; Figs 12d and 13b), whereas F2a and F3 had accumulated their near present-day lengths. Growth and linkage of the constituent segments of F2a, led to the formation of an extensional stepover and associated transtension related-depocenters (Figs 7c, and at 34 Ma in Fig. 12b). Given the presence of associate depocenter (Fig. 7c), the growth and overlap of F1a and F2a in the Eocene resulted in the formation of a extensional fault-dominated splay zone or relay between them (splay zone; Fig. 13b). During the Eocene-Oligocene (from 34 to 23 Ma; i.e. capturing 79 and 92% activity of the total F1a and F4a, and F2a-F3 history, respectively), many fault segments became inactive, with only a few segments (and a related transtensional depocentre) along and at the tip of F4a, and along the southern portion of F1a and F3, remaining active (Figs 7e-f and 11).

6.2.3 Miocene-Recent (23-0 Ma)

By the Miocene (from 23 to 5.3 Ma), F2a and F3 were inactive and had been buried by younger, post-rift sediment (Fig. 13c). In contrast, during this 17.7 Ma periods (capturing 95% activity of the total fault histories), the established segments along F4a-b and the southern portion of F1a continued to grow to their near present-day lengths, with several new segments forming at the end of 5.3 Ma (Figs 12a, d and 13c). The distribution of throw at the Albian level, which records the cumulative displacement on the faults through time, reveal that these established segments grew by solely lateral lengthening via tip propagation (ii-iv) and/or increasing in their maximum throw (v-vi, xvii-xix) (Fig. 12a, d and purple colour; Fig. 14a, d). As shown by multiple throw maxima at Albian or Eocene, and Miocene structural level (Fig. 11g-h and ab-ae), the maximum throw at the Miocene are interpreted to be related to dip-linkage reactivation due to nucleation of new fault segments at this strata. Given Upper Miocene-seabed strata thin toward salt diapirs SW2 and SW4 (Figs 7g-h), we suggest that fault reactivation reflect Miocene salt diapirism. This interpretation is supported by the structural restoration presented by Erdi and Jackson (2021), who show that SW2, which flanks F4a-b, underwent extension-driven fall and active rise since the Miocene. However, sinistral offsets are observed on some channels at top Upper Miocene (Figs 5c and 6e-f), thus dip-linkage related reactivation likely was contemporaneous with horizontal (i.e. translation) salt tectonic movement during Miocene. Subsequently, by the Miocene-Recent (last 5.3 Ma; i.e. last 5% of the total fault history), segment growth and/or diapirism induced the formation of transtensional graben, as clearly reflected by the formation of Miocene-seabed depocenters along the faults (Fig. 7g-h).

7 Discussion

7.1 Geometry and growth model of strike-slip faults

Numerous studies have focused the two-dimensional, typically map-view structure and related kinematics of strike-slip faults in various tectonic settings (e.g. Cunningham and Mann, 2007; Mann, 2007), with 2D seismic reflection data or single profiles from 3D volumes being used to illustrate their two-dimensional geometry (e.g. Harding, 1985; 1990; Leduc et al., 2012). Because of this, the three-dimensional geometry and related kinematic development of the strike-slip faults is poorly understood compared to, for example, normal faults (see reviews by Childs et al., 2017 and Rotevatn et al., 2019). Some field-based studies have described the four-dimensional patterns of strike-slip faulting, but again, due to outcrop limitations, these have largely focused on map-view patterns of, for example, throw; they have not, therefore, been able to directly deduce related dip-slip motions, or the dynamics of tip propagation and related fault linkage (Peacock, 1991; Kim et al., 2000; 2001; Nixon et al., 2011).

Three-dimensional seismic reflection data have relatively recently been employed to highlight the strike- and dip-slip components of motion on strike-slip faults. For example, Benesh et al. (2014) use 3D seismic reflection data from the Niger Delta to resolve the kinematics of linear, shale-detached strike-slip faults by mapping piercing points (i.e. deep-water channels and pre-existing thrust faults). They produced along-strike slip profiles by conducting map view-based surface restorations, revealing that strike-and dip-slip offsets and throws are not uniform along the faults. They did not, however, investigate the long-term kinematics of the faults. Deng et al (2019) use spatial variations in throws to determine the four-dimensional patterns of slip on segmented, strike-slip faults overlain by *en echelon* normal faults. They propose a model involving the growth of strike—slip faults by upward propagation of their tips and linkage with overlying faults.

Physical models have also been used to explore the kinematics of strike-slip faults above a crustal weak zone, showing that they initially formed segmented arrays of Riedel shear-like structures that propagated laterally and eventually hard-linked, resulting in the formation of restraining and/or releasing stepovers or bends (e.g., Dooley and Schreurs, 2012). More recently, Dooley et al. (2017) illustrate the formation, geometry, and kinematics of salt-detached strike-slip faults, showing that during basinward flow of salt and its overburden, different salt thicknesses across dip-parallel base-salt relief can generate parallel strike-slip faults in the overburden. The strike-slip faults form when the overburden is relatively thin, separating the faster translating, relatively thick salt domain from slower moving, relatively thin salt domain.

We used 3D seismic reflection data from the Outer Kwanza Basin, offshore Angola to determine the geometry and kinematics of salt-detached strike-slip fault arrays. Growth strata clearly indicate these structures nucleated in the Albian; however, the trigger for fault formation is less clear, given these structures likely formed 13-23 km updip of their present location, being subsequently translated seaward into their present positions. However, drawing on observations from physical models (Dooley et al., 2017) and other salt basins (e.g. Rowan et al., 1999; Fort and Brun, 2012), we speculate that the strike-slip faults formed to accommodate variable rates and magnitudes of overburden translation, related to base-salt related variations in salt thickness.

Using 3D seismic reflection data from the Outer Kwanza Basin, offshore Angola and a range of qualitative (i.e., isopach) and quantitative (i.e. lateral offset vs. distances and throw vs. distance and -depth plots, throw backstripping) fault analysis techniques, we are able to constrain the geometry and growth of a salt-detached strike-slip fault array. We show that these arrays initially consisted of several geometrically separate segments along which throw varied between normal and reverse motions (Fig. 8), consistent with the observations of Benesh et al (2019). These segments grew laterally via tip propagation, eventually linking with neighbouring segments (Fig. 12). Similar kinematics have been described from field-based studies (e.g. Peacock, 1991; Kim et al., 2000), and are simulated in physical models (e.g. Dooley and Schreurs, 2012). However, the excellent imaging and spatial coverage provided by our 3D seismic reflection dataset mean we are also able to show the key role played by dip-slip motions, and how these relates to the map-view evolution of the arrays, something that is difficult to do in exposures permitting only a 2D view of fault geometry (e.g. Peacock, 1991; Kim et al., 2000; 2001; Nixon et al., 2011). Our study shows that the evolution of these arrays was associated with the nucleation, and dip and strike propagation and linkage of segments experiencing coeval normal and/or reverse slip (Figs 12). Furthermore, throw-depth plots clearly show the upper tips of individual segments are characterised by consistently low throw gradients (Fig. 11e-f, m-n and z-aa), suggesting they were reactivated at some point in their history, and were not surface-breaching. This interpretation is consistent with that of Deng et al (2019), who also show that strike-slip faults need not always be surface-breaking. However, the presence of multiple throw maxima on throw-depth plots (Fig. 11c, g-h, l, u, y, ab-ae) suggest faults were also able to increase their height via reactivation and dip linkage with structures newly forming within shallower host rock.

7.2 Strike-slip fault scaling

Figure 14e shows a plot of maximum displacement-trace distance data for a global compilation of strike-slip faults, including the examples presented here from the Outer Kwanza Basin (Fig. 8). Our data fills a scale gap in the previous, global dataset (i.e., displacements of 10^2-10^3 m and distances of 10^3-10^4 m), lying within the overall scatter of these existing data. The scatter observed in our study may reflect measurement errors, sampling bias, and/or variations in the mechanical stratigraphy of the host (e.g. Kim and Sanderson, 2005; Torabi and Berg, 2011), although our backstripping results suggest it is a function of the growth or more specifically, the propagation and linkage history of the strike-slip faults (c.f. Cartwright et al., 1995) (Fig. 12). Our time-constrained analysis of how throw and distance (and their associated scaling relationship) change through time consistently show that the constituent segments (ii-xix) of the strike-slip fault arrays either: (i) attained their near-final lengths early during deformation, associated with lateral tip propagation and the linkage of adjacent segments (i.e., consistent with the constant-length model proposed for normal faults; e.g. Walsh et al., 2002) (label a; Fig. 14a-c); or (ii) grew via broadly synchronous increases in throw and length (i.e., consistent with the propagating fault model proposed for normal faults; e.g. Walsh and Watterson, 1988; Dawers et al., 1993) (label b; Fig. 14a-d). These observations suggest that scatter in the scaling relationships for strike-slip faults may simply reflect the fault growth process, in a similar way to that proposed for normal faults (e.g. Walsh and Watterson, 1988; Walsh et al., 2002).

8 Conclusions

We used 3D seismic reflection data from the Outer Kwanza Basin, Offshore Angola to determine the three-dimensional geometries and kinematics of salt-detached strike-slip faults. We show that deformation of Albian-to-Recent overburden above Aptian salt is locally accommodated by four, NE-SW-striking arrays that are up to 13 km long, 0.8 km tall, and which have normal and reverse throws of up to 617 m and 830 m, respectively. We speculate that these faults formed to accommodate along-strike variations in the rates and magnitudes of the salt-detached, seaward translation of overburden, possibly related to base-salt relief and related variations in salt thickness. Regardless of their origin, we show that the strike-slip arrays can be divided into several segments, defined by along-strike changes in the sense of throw, from normal to reverse. Our kinematic analysis reveals that faults nucleated sometime in the late Albian, with some segments establishing their near-final lengths during the initial 69% of their faulting history), whereas others attained their present-day length much later (i.e., after 95% of their faulting history). Fault growth, map-view changes in fault strike, and along-strike changes from normal to reverse throws resulted in the formation of releasing stepovers and restraining bends, whereas dip-slip motions resulted in fault reactivation and dip-linkage. The present-day throw-distance scaling relationships for the Outer Kwanza Basin fault arrays lie within the overall scatter of a global dataset, with some of the scatter within our dataset likely reflecting the fault growth process, in a similar way to that documented for normal faults. Our study provided a natural example of the geometry and kinematics of strike-slip faults on a salt-bearing passive margin, showing the integral roles of strike- and dip-linkage in their development. These learnings may be applicable to similar faults forming within intraplate settings.

Acknowledgement

We wish to thank Joe Cartwright, Mark Rowan, Timothy Wigan and Bailey Lathrop for discussions during the course of this study. A big thank you to CGG for providing access to the high-quality 3D seismic dataset and for allowing publication of the results of this study. This study is a PhD study of the first author, who is sponsored by Indonesia Endowment Fund for Education (LPDP). The first author would also like to thank the Research Center for Geotechnology, Indonesian Institute of Science (LIPI) (now National Research and Innovation Agency - BRIN), Indonesia for indirect assistance and administrative support during his PhD research. All authors acknowledge Schlumberger for providing Petrel software to Imperial College London.

Table Captions

Table 1: Summary of structural and stratigraphy features in sub-domains that are separated by salt detached strike-slip faults (see Figure 5).

Figure Captions

Figure 1: Schematic diagrams illustrating the geometry and kinematics of salt-detached strike-slip faults. (a) A synoptic model (modified from Rowan et al., 1999). (b) An example from the Levant Basin, offshore Israel (modified from Cartwright et al., 2012). (c) An example from the northern Gulf of Mexico (Rowan et al., 1999). (d) An example from the northern Gulf of Mexico (modified from Fort and Brun, 2012). (e) An example from a physical model, highlighting the

key role on base-salt relief and salt thickness on fault development and geometry (modified from Dooley et al., 2017).

Figure 2: A simplified map and cross section of the Offshore Angola region, with the approximate location of our study area indicated by the red box. (a) A regional map illustrating the key tectonic features and salt tectonic domains in the Offshore Angola. (b) A semi-regional cross-section showing the presence of salt-detached strike-slip faults above the Aptian salt layer. The salt layer is confined by an underlying, rift-related structural high (SH) and a crustal-scale transfer fault zone (modified from Erdi and Jackson, 2021).

Figure 3: Schematic diagram illustrating the nomenclature and techniques used to determine the geometry of strike-slip faults in this study. (a) oblique view of a strike-slip fault; (b) displacement contours on a fault surface; (c) a lateral offset vs. throw displacement profile; (d) a hypothetical two-dimensional cross-section of a master strike-slip fault; (e) a throw-depth profile across a fault; (f) an expansion indices plot.

Figure 4: Uninterpreted and interpreted of (a) base-salt, and (b) salt thickness maps. Both (a) and (b) are overlaid to create (c), a composite sketch map showing how salt thickness and base-salt depth relate. These maps illustrate that salt anticlines (SA), wall (SW), squeezed walls (SQ), and anticlines (SN), and salt-detached strike-slip fault arrays *presently* occur parallel to and above NE-, N-, NE-trending base-salt relief (ramps).

Figure 5: Uninterpreted and interpreted variance attribute maps at (a) the top of Albian, (b) the top of Eocene, and (c) the top of Miocene structures, illustrating the geometry of several strike-slip fault arrays (F1-F5) at each structural level. Note that these arrays define the margins of structural domains defined by different styles and intensities of salt-related deformation (see Table 1 for full description of each zone). Seismic data courtesy of CGG Earth data (previously CGG Multi-Client).

Figure 6: Zoom-in of a variance map, showing the detailed geometry of NE-trending, salt-detached strike-slip faults (F1-F4) between the (a-b) Albian, (c-d) Eocene, and (e-f) Upper Miocene structural levels (see map location shown in Figure 5; see also Figure S4-S5 in Appendix C for uninterpreted and interpretative sketch of variance attribute maps). Seismic data courtesy of CGG Earth data (previously CGG Multi-Client).

Figure 7: Interpreted isopach maps (contour interval of 100 m) for the (a-b) Aptian-Albian, (c-d) Albian-Eocene, (e-f) Eocene-Oligocene, (g-h) Upper Miocene to seabed intervals, showing thickness patterns adjacent along the strike-slip fault arrays (F1-F5) and significant salt structures (SW2 and SW4) (see map location in Figure 5; see also Figure S6-S7 in Appendix C for uninterpreted and interpretative sketch of isopach maps).

Figure 8: Composite thickness variation (derived from isopach maps; see Fig. 7) and displacement-distance graphs for strike-slip faults (a) F1a, (b) F2a, (c) F3, and (d) F4a, b (see Table S1-S2 in Appendix D for raw data of displacement-distance). The displacement-distance graphs consist of two plots; maximum lateral offset (LO; right side) and throw (TH; left side). The maximum lateral offsets (purple color) are constrained by piercing points (i.e. salt diapir, anticline and channels), whereas throws are constrained by the vertical separation of the Albian (blue), Eocene (orange), and Upper Miocene (yellow) seismic reflections. The location of prominent base-salt relief is shown in black. The locations of pop up-related stratal thinning and transtension-depocenters (as defined on Albian, Eocene and Upper Miocene isopach maps; see Fig. 7) are also shown, reflecting the distribution of restraining bends and releasing stepovers along the faults.

Figure 9: Seismic profiles across each strike-slip fault-bound structural domain (profile locations shown in Figures 4a, b and 5a; see also Figure S2 in Appendix B for uninterpreted cross sections) (Erdi and Jackson, 2021). (a) salt anticlines (SA4-6) in the northwest of the study area; (b) a squeezed salt anticline (SN1b), wall (SQ1), and roller (unnamed) in the center of the study area; (c) salt anticlines (SA1-3), a squeezed wall (SQ2a), and a roller (unnamed) in the center of the study area; (d) fore- and back-thrusts above a squeezed salt wall (SQ2b), and a reactive salt wall (SW2). Seismic data courtesy of CGG Earth data (previously CGG Multi-Client).

Figure 10: Seismic profiles illustrating the two-dimensional structural style of salt-detached strike-slip faults arrays (F1-F4) (profile locations shown in Figures 4a, b, 5a and 8; see also Figure S3 in Appendix B for uninterpreted cross sections). (a) F1a, showing a planar cross-sectional geometry and normal throws above a primary weld. (b) F1a in a more seaward (i.e., south-westerly) position compared to (a), showing normal throws at the Albian structural level, but reverse throws at the Eocene structural level. (c) F1a in a more seaward (i.e., south-westerly) position to (b), displaying reverse throws at all structural levels; F2a is planar and displays

normal throws. (d) 0.5 km seaward of (c), F1a and F2a display normal throws and bound negative flower structures. (e) 2 km seaward of (d), F1a displays reverse throws, whereas F2a persistently display negative flower structures. (f) F3, showing a planar cross-sectional geometry and normal throws at Albian-Lower Miocene structural levels; F4a bounds negative flower structures and normal throws at Albian-Seabed structural levels. (g) 3.6 km seaward of (f), F4 is defined by soft-linkage between F4a and F4b, and the oppositely dipping (i.e., antithetic) array, F4c. Note that the strike-slip faults are located above either base-salt highs or areas in which the base-salt is flat. Seismic data courtesy of CGG Earth data (previously CGG Multi-Client).

Figure 11: Throw-depth (T-z) and corresponding expansion indices plots for the (a-i) F1a, (j-r) F2a, (s-aa) F3, and (ab-ag) F4a arrays (see their corresponding location on displacement-distance in Fig. 8). The location of maximum throw is labelled (label 1-3). Note that throw varies along-strike and the faults upper tips are characterized by low throw gradients. EI plots show a broadly positive correlation between EI values >1 (i.e. thickening-into-the-hangingwall) and areas of normal throw (labelled “i”), and EI values <1 (thickening-into-the-footwall) and areas of reverse throw (labelled “ii”). Areas where EI values >1 are associated with reverse throws are also seen, with this inferred to record the across-fault juxtaposition of depocenters due to strike-slip motions on faults bounding previously geographically separate depocentres (labelled “iii”).

Figure 12: Backstripping of composite throw-distance and isopach maps for (a) F1, (b) F2, (c) F3 and (d) F4 array. Note that these backstripping data show the evolution of throw at the top Albian structural level, illustrating the formation of restraining bends and releasing stepovers (taken from Figure 7) at 100. 5 Ma (i.e., after 11-13% of the faulting history), 34 Ma (i.e., after 69-81% of the faulting history), and 5 Ma (i.e., after 95% of the faulting history). Backstripping used the maximum throw subtraction method (e.g. Rowan et al., 1998; see also Appendix A2 for full explanation).

Figure 13: Schematic map-view and cross-sectional reconstruction showing the interpreted evolution of strike-slip faults arrays at (a) 100.5 Ma, (b) 34 Ma, and (c) 5 Ma.

Figure 14: Throw-distance trajectory plots for (a) F1a, (b) F2a, (c) F3, and (d) F4 since 100. 5 Ma (see each segment in Fig. 8 and their corresponding evolution in Fig. 12). In (e) we plot our lateral offset vs. displacement data from array of F1-F4 against a global dataset of lateral

displacement-length for strike-slip faults (see Table S3 in Appendix D for raw data). The inset shows a zoom-in of the lateral offset vs. distance.

Data Availability Statement

The seismic data supporting the findings of this study are available from CGG. However, restrictions apply to the availability of these data, which were used under license for this study.

References

Bahorich, M., & Farmer, S. (1995). 3-D seismic discontinuity for faults and stratigraphic features: The coherence cube. *The Leading Edge, 14*(10), 1053-1058. doi:10.1190/1.1437077

Bates, R. L., & Jackson, J. A. (1997). *Glossary of geology*. Alexandria, Viriginia: American Geological Institute.

Baudon, C., & Cartwright, J. (2008). The kinematics of reactivation of normal faults using high resolution throw mapping. *Journal of Structural Geology, 30*(8), 1072-1084. doi:10.1016/j.jsg.2008.04.008

Benesh, N. P., Plesch, A., & Shaw, J. H. (2014). Geometry, kinematics, and displacement characteristics of tear-fault systems: An example from the deep-water Niger Delta. *AAPG Bulletin, 98*(3), 465-482. doi:10.1306/06251311013

Bergen, K. J., & Shaw, J. H. (2010). Displacement profiles and displacement-length scaling relationships of thrust faults constrained by seismic-reflection data. *GSA Bulletin, 122*(7-8), 1209-1219. doi:10.1130/B26373.1

Bull, S., Cartwright, J., & Huuse, M. (2009). A review of kinematic indicators from mass-transport complexes using 3D seismic data. *Marine and Petroleum Geology, 26*(7), 1132-1151. doi:https://doi.org/10.1016/j.marpetgeo.2008.09.011

Cartwright, J., Jackson, M., Dooley, T., & Higgins, S. (2012). Strain partitioning in gravity-driven shortening of a thick, multilayered evaporite sequence. *Geological Society, London, Special Publications, 363*(1), 449.

Cartwright, J. A., & Mansfield, C. S. (1998). Lateral displacement variation and lateral tip geometry of normal faults in the Canyonlands National Park, Utah. *Journal of Structural Geology, 20*(1), 3-19. doi:10.1016/s0191-8141(97)00079-5

Cartwright, J. A., Trudgill, B. D., & Mansfield, C. S. (1995). Fault growth by segment linkage: an explanation for scatter in maximum displacement and trace length data from the Canyonlands Grabens of SE Utah. *Journal of Structural Geology, 17*(9), 1319-1326. doi:10.1016/0191-8141(95)00033-a

Chapman, T. J., & Meneilly, A. W. (1991). The displacement patterns associated with a reverse-reactivated, normal growth fault. *Geological Society, London, Special Publications, 56*(1), 183-191. doi:10.1144/gsl.sp.1991.056.01.12

Childs, C., Holdsworth, R. E., Jackson, C. A. L., Manzocchi, T., Walsh, J. J., & Yielding, G. (2017). Introduction to the geometry and growth of normal faults. *Geological Society, London, Special Publications, 439*. Retrieved from http://sp.lyellcollection.org/content/early/2017/09/05/SP439.24.abstract

Christie-Blick, N., & Biddle, K. T. (1985). Deformation and Basin Formation along Strike-Slip Faults1. In K. T. Biddle & N. Christie-Blick (Eds.), *Strike-Slip Deformation, Basin Formation, and Sedimentation* (Vol. 37, pp. 0). doi:10.2110/pec.85.37.0001

Cunningham, W. D., & Mann, P. (2007). Tectonics of strike-slip restraining and releasing bends. *Geological Society, London, Special Publications, 290*(1), 1. doi:10.1144/SP290.1

Dawers, N. H., Anders, M. H., & Scholz, C. H. (1993). Growth of normal faults: Displacement-length scaling. *Geology, 21*(12), 1107. doi:10.1130/0091-7613(1993)021<1107:gonfdl>2.3.co;2

de Joussineau, G., & Aydin, A. (2009). Segmentation along Strike-Slip Faults Revisited. 1575-1594. doi:10.1007/978-3-0346-0138-2_3

Deng, S., Li, H., Zhang, Z., Zhang, J., & Yang, X. (2019). Structural characterization of intracratonic strike-slip faults in the central Tarim Basin. *AAPG Bulletin, 103*(1), 109-137. doi:10.1306/06071817354

Dooley, T. P., Hudec, M. R., Carruthers, D., Jackson, M. P. A., & Luo, G. (2017). The effects of base-salt relief on salt flow and suprasalt deformation patterns — Part 1: Flow across simple steps in the base of salt. *Interpretation, 5*(1), SD1-SD23. doi:10.1190/int-2016-0087.1

Dooley, T. P., & Schreurs, G. (2012). Analogue modelling of intraplate strike-slip tectonics: A review and new experimental results. *Tectonophysics, 574-575*, 1-71. doi:10.1016/j.tecto.2012.05.030

Dutton, D. M., & Trudgill, B. D. (2009). Four-dimensional analysis of the Sembo relay system, offshore Angola: Implications for fault growth in salt-detached settings. *AAPG Bulletin, 93*(6), 763-794. doi:10.1306/02230908094

Duval, B., Cramez, C., & Jackson, M. P. A. (1992). Raft tectonics in the Kwanza Basin, Angola. *Marine and Petroleum Geology, 9*(4), 389-404. doi:10.1016/0264-8172(92)90050-o

Erdi, A., & Jackson, C. A. L. (2021). What controls salt-detached contraction in the translational domain of the outer Kwanza Basin, offshore Angola? *Basin Research, 33*(3), 1880-1905. doi:10.1111/bre.12539

Escalona, A., & Mann, P. (2006). Tectonic controls of the right-lateral Burro Negro tear fault on Paleogene structure and stratigraphy, northeastern Maracaibo Basin. *AAPG Bulletin, 90*(4), 479-504. doi:10.1306/10070505032

Evans, S. L., & Jackson, C. A. L. (2019). Base-salt relief controls salt-related deformation in the Outer Kwanza Basin, offshore Angola. *Basin Research, 32*(4), 668-687. doi:10.1111/bre.12390

Fernandez, N., Duffy, O. B., Peel, F. J., & Hudec, M. R. (2020). Influence of minibasin obstruction on canopy dynamics in the northern Gulf of Mexico. *Basin Research, 33*(1), 427-446. doi:10.1111/bre.12480

Fort, X., & Brun, J.-P. (2012). Kinematics of regional salt flow in the northern Gulf of Mexico. *Geological Society, London, Special Publications, 363*(1), 265. doi:10.1144/SP363.12

Fu, B., & Awata, Y. (2007). Displacement and timing of left-lateral faulting in the Kunlun Fault Zone, northern Tibet, inferred from geologic and geomorphic features. *Journal of Asian Earth Sciences*, *29*(2), 253-265. doi:https://doi.org/10.1016/j.jseaes.2006.03.004

Guiraud, M., Buta-Neto, A., & Quesne, D. (2010). Segmentation and differential post-rift uplift at the Angola margin as recorded by the transform-rifted Benguela and oblique-to-orthogonal-rifted Kwanza basins. *Marine and Petroleum Geology, 27*(5), 1040-1068. doi:10.1016/j.marpetgeo.2010.01.017

Harding, T. P. (1985). Seismic Characteristics and Identification of Negative Flower Structures, Positive Flower Structures, and Positive Structural Inversion1. *AAPG Bulletin, 69*(4), 582-600. doi:10.1306/AD462538-16F7-11D7-8645000102C1865D

Harding, T. P. (1990). Identification of Wrench Faults Using Subsurface Structural Data: Criteria and Pitfalls1. *AAPG Bulletin, 74*(10), 1590-1609. doi:10.1306/0C9B2533-1710-11D7-8645000102C1865D

Higgins, S., Clarke, B., Davies, R. J., & Cartwright, J. (2009). Internal geometry and growth history of a thrust-related anticline in a deep water fold belt. *Journal of Structural Geology, 31*(12), 1597-1611. doi:https://doi.org/10.1016/j.jsg.2009.07.006

Hudec, M. R., & Jackson, M. P. A. (2002). Structural segmentation, inversion, and salt tectonics on a passive margin: Evolution of the Inner Kwanza Basin, Angola. *Geological Society of America Bulletin, 114*(10), 1222-1244. doi:10.1130/0016-7606(2002)114<1222:ssiast>2.0.co;2

Hudec, M. R., & Jackson, M. P. A. (2004). Regional restoration across the Kwanza Basin, Angola: Salt tectonics triggered by repeated uplift of a metastable passive margin. *AAPG Bulletin, 88*(7), 971-990. doi:10.1306/02050403061

Jachens, R. C., Langenheim, V. E., & Matti, J. C. (2002). Relationship of the 1999 Hector Mine and 1992 Landers Fault Ruptures to Offsets on Neogene Faults and Distribution of Late Cenozoic Basins in the Eastern California Shear Zone. *Bulletin of the Seismological Society of America, 92*(4), 1592-1605. doi:10.1785/0120000915

Jackson, C. A. L., Bell, R. E., Rotevatn, A., & Tvedt, A. B. M. (2017). Techniques to determine the kinematics of synsedimentary normal faults and implications for fault growth models. *Geological Society, London, Special Publications, 439*(1), 187-217. doi:10.1144/sp439.22

Jackson, C. A. L., & Rotevatn, A. (2013). 3D seismic analysis of the structure and evolution of a salt-influenced normal fault zone: A test of competing fault growth models. *Journal of Structural Geology, 54*, 215-234. doi:10.1016/j.jsg.2013.06.012

Jackson, M. P. A., & Hudec, M. R. (2005). Stratigraphic record of translation down ramps in a passive-margin salt detachment. *Journal of Structural Geology, 27*(5), 889-911. doi:10.1016/j.jsg.2005.01.010

Kim, Y.-S., Andrews, J. R., & Sanderson, D. J. (2000). Damage zones around strike-slip fault systems and strike-slip fault evolution, Crackington Haven, southwest England. *Geosciences Journal, 4*(2), 53. doi:10.1007/BF02910127

Kim, Y.-S., Andrews, J. R., & Sanderson, D. J. (2001). Reactivated strike–slip faults: examples from north Cornwall, UK. *Tectonophysics, 340*(3-4), 173-194. doi:10.1016/s0040-1951(01)00146-9

Kim, Y.-S., Peacock, D. C. P., & Sanderson, D. J. (2004). Fault damage zones. *Journal of Structural Geology, 26*(3), 503-517. doi:https://doi.org/10.1016/j.jsg.2003.08.002

Kim, Y.-S., & Sanderson, D. J. (2005). The relationship between displacement and length of faults: a review. *Earth-Science Reviews, 68*(3-4), 317-334. doi:10.1016/j.earscirev.2004.06.003

Leduc, A. M., Davies, R. J., Densmore, A. L., & Imber, J. (2012). The lateral strike-slip domain in gravitational detachment delta systems: A case study of the northwestern margin of the Niger Delta. *AAPG Bulletin, 96*(4), 709-728. doi:10.1306/09141111035

Lundin, E. R. (1992). Thin-skinned extensional tectonics on a salt detachment, northern Kwanza Basin, Angola. *Marine and Petroleum Geology, 9*(4), 405-411. doi:10.1016/0264-8172(92)90051-f

Mann, P. (2007). Global catalogue, classification and tectonic origins of restraining- and releasing bends on active and ancient strike-slip fault systems. *Geological Society, London, Special Publications, 290*(1), 13. doi:10.1144/SP290.2

Mansfield, C. S., & Cartwright, J. A. (1996). High resolution fault displacement mapping from three-dimensional seismic data: evidence for dip linkage during fault growth. *Journal of Structural Geology, 18*(2), 249-263. doi:https://doi.org/10.1016/S0191-8141(96)80048-4

Marton, L. G., Tari, G. C., & Lehmann, C. T. (2000). Evolution of the Angolan passive margin, West Africa, with emphasis on post-salt structural styles. *Atlantic Rifts and Continental Margins, 115*, 129-149. doi:10.1029/GM115p0129

Maurin, J.-C., & Guiraud, R. (1993). Basement control in the development of the early cretaceous West and Central African rift system. *Tectonophysics, 228*(1), 81-95. doi:https://doi.org/10.1016/0040-1951(93)90215-6

McMillan, R. A. (1975). *The orientation and sense of displacement of strike–slip faults in continental crust.* (Bachelor). Carleton University, Ottawa, Ontario.

Moulin, M., Aslanian, D., Olivet, J.-L., Contrucci, I., Matias, L., Géli, L., . . . Unternehr, P. (2005). Geological constraints on the evolution of the Angolan margin based on reflection and refraction seismic data (ZaïAngo project). *Geophysical Journal International, 162*(3), 793-810. doi:10.1111/j.1365-246X.2005.02668.x

Nemer, T., & Meghraoui, M. (2006). Evidence of coseismic ruptures along the Roum fault (Lebanon): a possible source for the AD 1837 earthquake. *Journal of Structural Geology, 28*(8), 1483-1495. doi:https://doi.org/10.1016/j.jsg.2006.03.038

Nicol, A., Childs, C., Walsh, J. J., Manzocchi, T., & Schöpfer, M. P. J. (2017). Interactions and growth of faults in an outcrop-scale system. *Geological Society, London, Special Publications, 439*(1), 23. doi:10.1144/SP439.9

Nicol, A., Watterson, J., Walsh, J. J., & Childs, C. (1996). The shapes, major axis orientations and displacement patterns of fault surfaces. *Journal of Structural Geology, 18*(2), 235-248. doi:https://doi.org/10.1016/S0191-8141(96)80047-2

Nixon, C. W., Sanderson, D. J., & Bull, J. M. (2011). Deformation within a strike-slip fault network at Westward Ho!, Devon U.K.: Domino vs conjugate faulting. *Journal of Structural Geology, 33*(5), 833-843. doi:10.1016/j.jsg.2011.03.009

Omosanya, K. O., Zervas, I., Mattos, N. H., Alves, T. M., Johansen, S. E., & Marfo, G. (2017). Strike-Slip Tectonics in the SW Barents Sea During North Atlantic Rifting (Swaen Graben, Northern Norway). *Tectonics, 36*(11), 2422-2446. doi:10.1002/2017TC004635

Pan, S., Bell, R. E., Jackson, C. A. L., & Naliboff, J. (2022). Evolution of normal fault displacement and length as continental lithosphere stretches. *Basin Research, 34*(1), 121-140. doi:https://doi.org/10.1111/bre.12613

Peacock, D. C. P. (1991). Displacements and segment linkage in strike-slip fault zones. *Journal of Structural Geology, 13*(9), 1025-1035. doi:10.1016/0191-8141(91)90054-m

Peacock, D. C. P., & Sanderson, D. J. (1994). Geometry and Development of Relay Ramps in Normal Fault Systems. *AAPG Bulletin, 78*(2), 147-165. doi:10.1306/BDFF9046-1718-11D7-8645000102C1865D

Peacock, D. C. P., & Sanderson, D. J. (1995). Strike-slip relay ramps. *Journal of Structural Geology, 17*(10), 1351-1360. doi:10.1016/0191-8141(95)97303-w

Pichel, L. M., Jackson, C. A. L., Peel, F., & Dooley, T. P. (2019). Base-salt relief controls salt-tectonic structural style, São Paulo Plateau, Santos Basin, Brazil. *Basin Research, 32*(3), 453-484. doi:10.1111/bre.12375

Reeve, M. T., Bell, R. E., Duffy, O. B., Jackson, C. A. L., & Sansom, E. (2015). The growth of non-colinear normal fault systems; What can we learn from 3D seismic reflection data? *Journal of Structural Geology, 70*, 141-155. doi:10.1016/j.jsg.2014.11.007

Rotevatn, A., Jackson, C. A. L., Tvedt, A. B. M., Bell, R. E., & Blækkan, I. (2019). How do normal faults grow? *Journal of Structural Geology, 125*, 174-184. doi:https://doi.org/10.1016/j.jsg.2018.08.005

Rovida, A., & Tibaldi, A. (2005). Propagation of strike-slip faults across Holocene volcano-sedimentary deposits, Pasto, Colombia. *Journal of Structural Geology, 27*(10), 1838-1855. doi:https://doi.org/10.1016/j.jsg.2005.06.009

Rowan, M. G., Hart, B. S., Nelson, S., Flemings, P. B., & Trudgill, B. D. (1998). Three-dimensional geometry and evolution of a salt-related growth-fault array: Eugene Island 330 field, offshore Louisiana, Gulf of Mexico. *Marine and Petroleum Geology, 15*(4), 309-328. doi:10.1016/s0264-8172(98)00021-x

Rowan, M. G., Jackson, M. P. A., & Trudgill, B. D. (1999). Salt-Related Fault Families and Fault Welds in the Northern Gulf of Mexico. *AAPG Bulletin, 83*(9), 1454-1484. doi:10.1306/e4fd41e3-1732-11d7-8645000102c1865d

Scholz, C. H., & Cowie, P. A. (1990). Determination of total strain from faulting using slip measurements. *Nature, 346*(6287), 837-839. doi:10.1038/346837a0

Sieh, K., & Natawidjaja, D. (2000). Neotectonics of the Sumatran fault, Indonesia. *Journal of Geophysical Research: Solid Earth, 105*(B12), 28295-28326. doi:https://doi.org/10.1029/2000JB900120

Sylvester, A. G. (1988). Strike-slip faults. *GSA Bulletin, 100*(11), 1666-1703. doi:10.1130/0016-7606(1988)100<1666:SSF>2.3.CO;2

Tatar, O., Piper, J. D. A., Gürsoy, H., Heimann, A., & Koçbulut, F. (2004). Neotectonic deformation in the transition zone between the Dead Sea Transform and the East Anatolian Fault Zone, Southern Turkey: a palaeomagnetic study of the Karasu Rift Volcanism. *Tectonophysics, 385*(1), 17-43. doi:https://doi.org/10.1016/j.tecto.2004.04.005

Thorsen, C. E. (1963). Age of growth faulting in south-east Louisiana. *Gulf Costs Association of Geologists Societies Transactions, 13*, 103-110.

Torabi, A., & Berg, S. S. (2011). Scaling of fault attributes: A review. *Marine and Petroleum Geology, 28*(8), 1444-1460. doi:10.1016/j.marpetgeo.2011.04.003

Tvedt, A. B. M., Rotevatn, A., & Jackson, C. A. L. (2016). Supra-salt normal fault growth during the rise and fall of a diapir: Perspectives from 3D seismic reflection data, Norwegian North Sea. *Journal of Structural Geology, 91*, 1-26. doi:10.1016/j.jsg.2016.08.001

Von Nicolai, C. (2011). *The Interplay of Salt Movements and Regional Tectonics at the Passive Continental Margin of the South Atlantic, Kwanza Basin.* (PhD thesis). Universität Potsdam, Retrieved from [https ://goo.gl/8LwQBY]

Wagner, B. H., & Jackson, M. P. A. (2011). Viscous flow during salt welding. *Tectonophysics, 510*(3-4), 309-326. doi:10.1016/j.tecto.2011.07.012

Walker, R., & Jackson, J. (2002). Offset and evolution of the Gowk fault, S.E. Iran: a major intra-continental strike-slip system. *Journal of Structural Geology, 24*(11), 1677-1698. doi:https://doi.org/10.1016/S0191-8141(01)00170-5

Walsh, J. J., Nicol, A., & Childs, C. (2002). An alternative model for the growth of faults. *Journal of Structural Geology, 24*(11), 1669-1675. doi:https://doi.org/10.1016/S0191-8141(01)00165-1

Walsh, J. J., & Watterson, J. (1988). Analysis of the relationship between displacements and dimensions of faults. *Journal of Structural Geology*, *10*(3), 239-247. doi:https://doi.org/10.1016/0191-8141(88)90057-0

Walsh, J. J., & Watterson, J. (1989). Displacement gradients on fault surfaces. *Journal of Structural Geology*, *11*(3), 307-316. doi:https://doi.org/10.1016/0191-8141(89)90070-9

Wesnousky, S. G. (1988). Seismological and structural evolution of strike-slip faults. *Nature*, *335*(6188), 340-343. doi:10.1038/335340a0

Table

Table 1

Structural level	Sub-domain	Description of deformation and stratigraphic features
Albian and Eocene	1	A high degree deformation domain, being reflected by: ▪ Four NW-trending salt anticlines (SA4-7) ▪ Two NW-trending salt-detached thrust faults ▪ Up to seventeen N- or NE-trending salt-detached normal faults
	2	A relatively low degree deformation domain, being reflected by: ▪ a NW-trending salt anticline and squeezed diapir (SN1a) ▪ Up to eleven N-trending salt-detached normal faults
	3	A high degree deformation domain, being reflected by: ▪ Up to thirteen NW-, N- or NE-trending salt anticlines (SA1) ▪ Up to fourty nine NW- or NE-trending salt-detached normal fault
	4	A relatively moderate-high degree deformation domain, being reflected by: ▪ Five NW- or N-trending salt anticlines, and squeeze diapir (SN1b and SQ1) ▪ Up to twenty N- or NE-trending salt-detached normal faults
	5	A relatively low degree of deformation domain, being reflected by: ▪ Two NW- or W-trending, salt anticline (SA3) and squeezed diapir (SQ2a) ▪ Up to ten NW- or N-trending salt-detached normal faults
	6	A relatively low degree of deformation domain, being reflected by: ▪ a NW-trending squeezed diapir (SQ2b) ▪ Up to four NW-trending salt-detached normal faults
Upper Miocene	1	A relatively low degree deformation domain, being reflected by: ▪ Three NW-trending salt-detached normal faults ▪ A NW-trending channel
	2 3 4 5	A relatively low-moderate degree of deformation domain, being reflected by: ▪ Up to seventeen NW-trending salt-detached normal faults ▪ Five W-, NW-, or N-trending channels
	6	A relatively no particular deformation domain, being reflected by: ▪ A W-trending channel

Figures

Figure 1

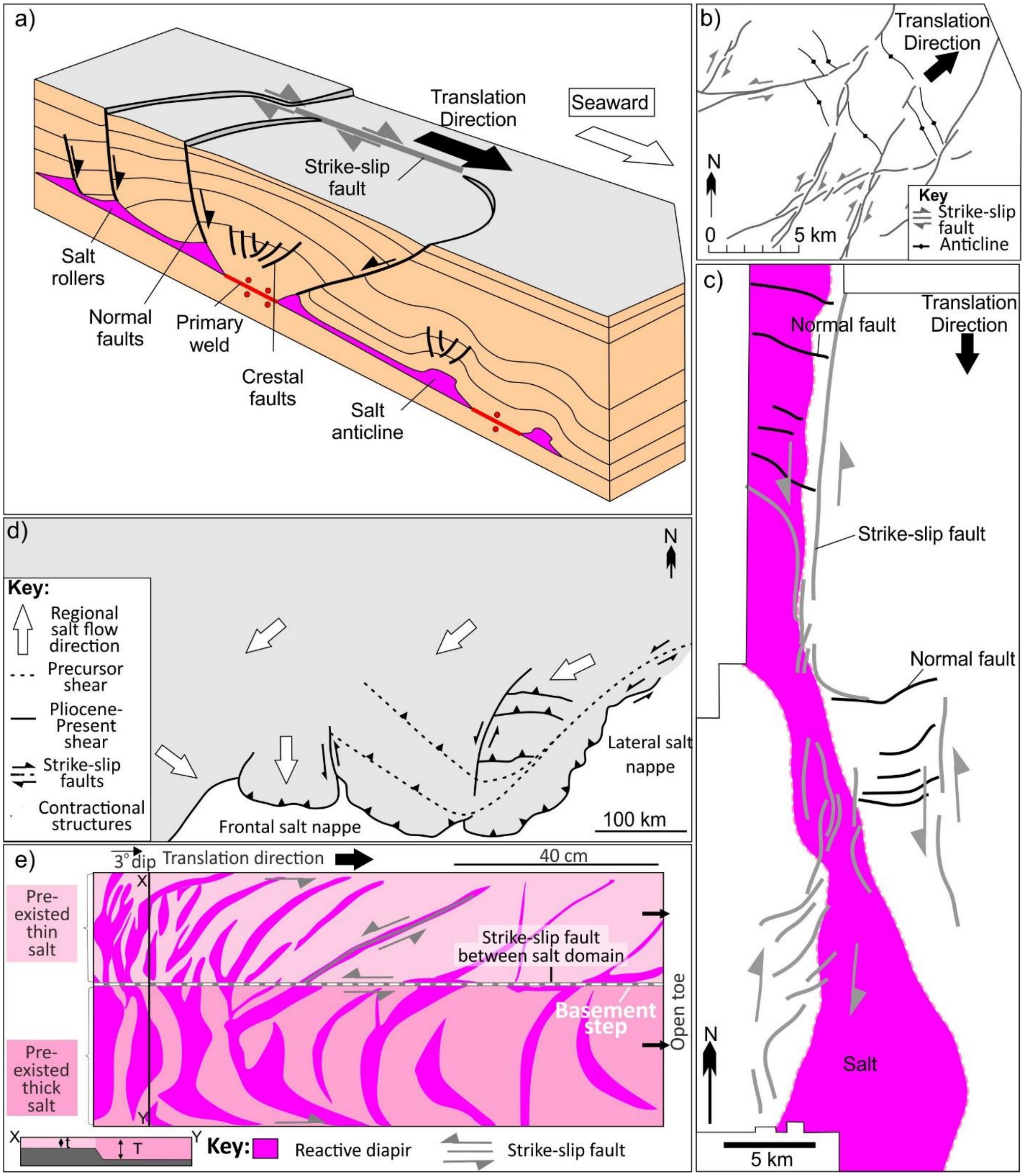

Figure 2

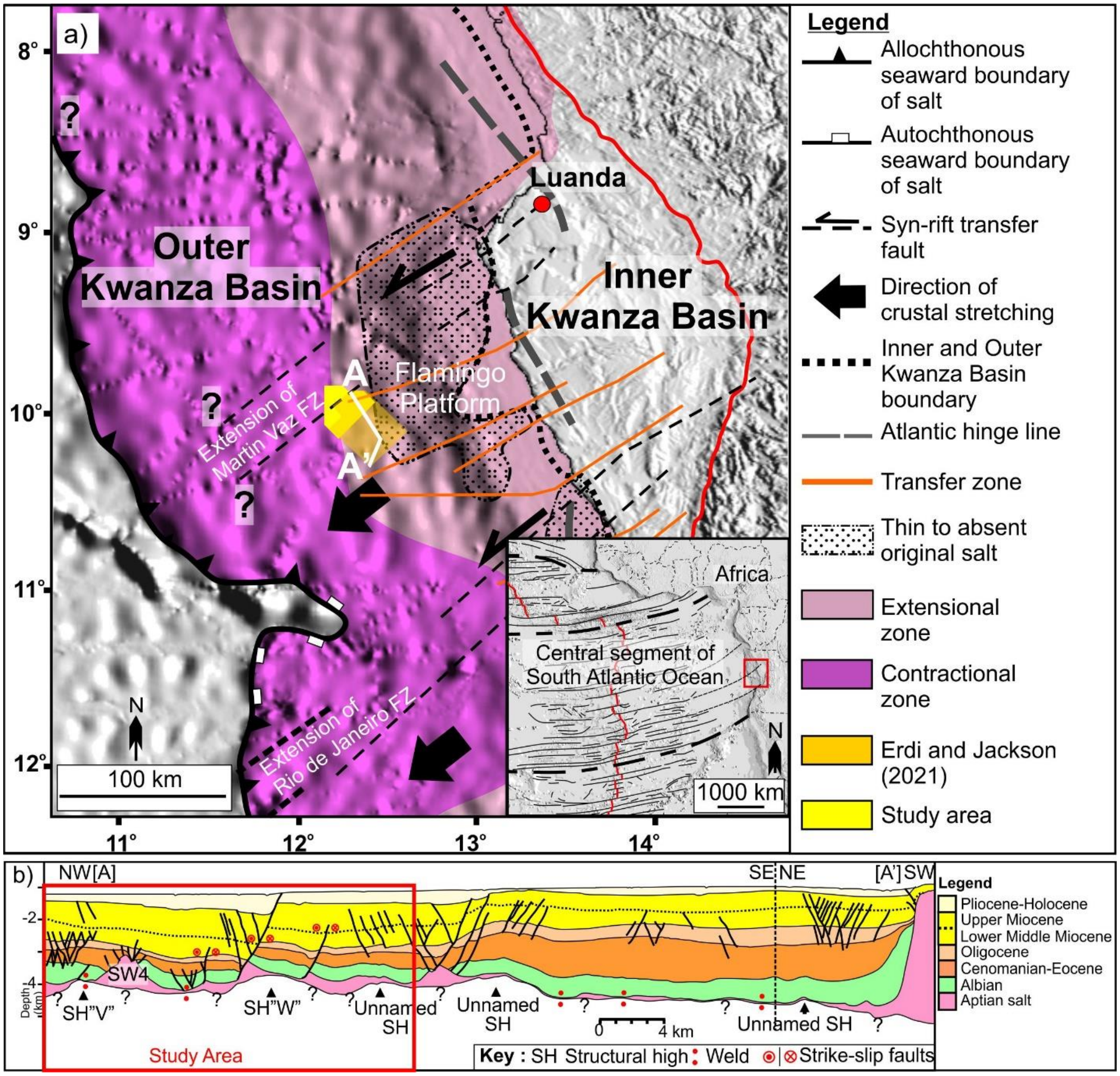

a)
8°
9°
10°
11°
12°
11°
12°
13°
14°
Outer Kwanza Basin
Inner Kwanza Basin
Luanda
Flamingo Platform
A
A'
Extension of Martin Vaz FZ
Extension of Rio de Janeiro FZ
100 km
N
Africa
Central segment of South Atlantic Ocean
1000 km
Legend
Allochthonous seaward boundary of salt
Autochthonous seaward boundary of salt
Syn-rift transfer fault
Direction of crustal stretching
Inner and Outer Kwanza Basin boundary
Atlantic hinge line
Transfer zone
Thin to absent original salt
Extensional zone
Contractional zone
Erdi and Jackson (2021)
Study area
b)
NW[A]
SE NE
[A'] SW
-2
-4
Depth (km)
SW4
SH"V"
SH"W"
Unnamed SH
Unnamed SH
Unnamed SH
0
4 km
Study Area
Key : SH Structural high Weld Strike-slip faults
Legend
Pliocene-Holocene
Upper Miocene
Lower Middle Miocene
Oligocene
Cenomanian-Eocene
Albian
Aptian salt

912 Figure 3

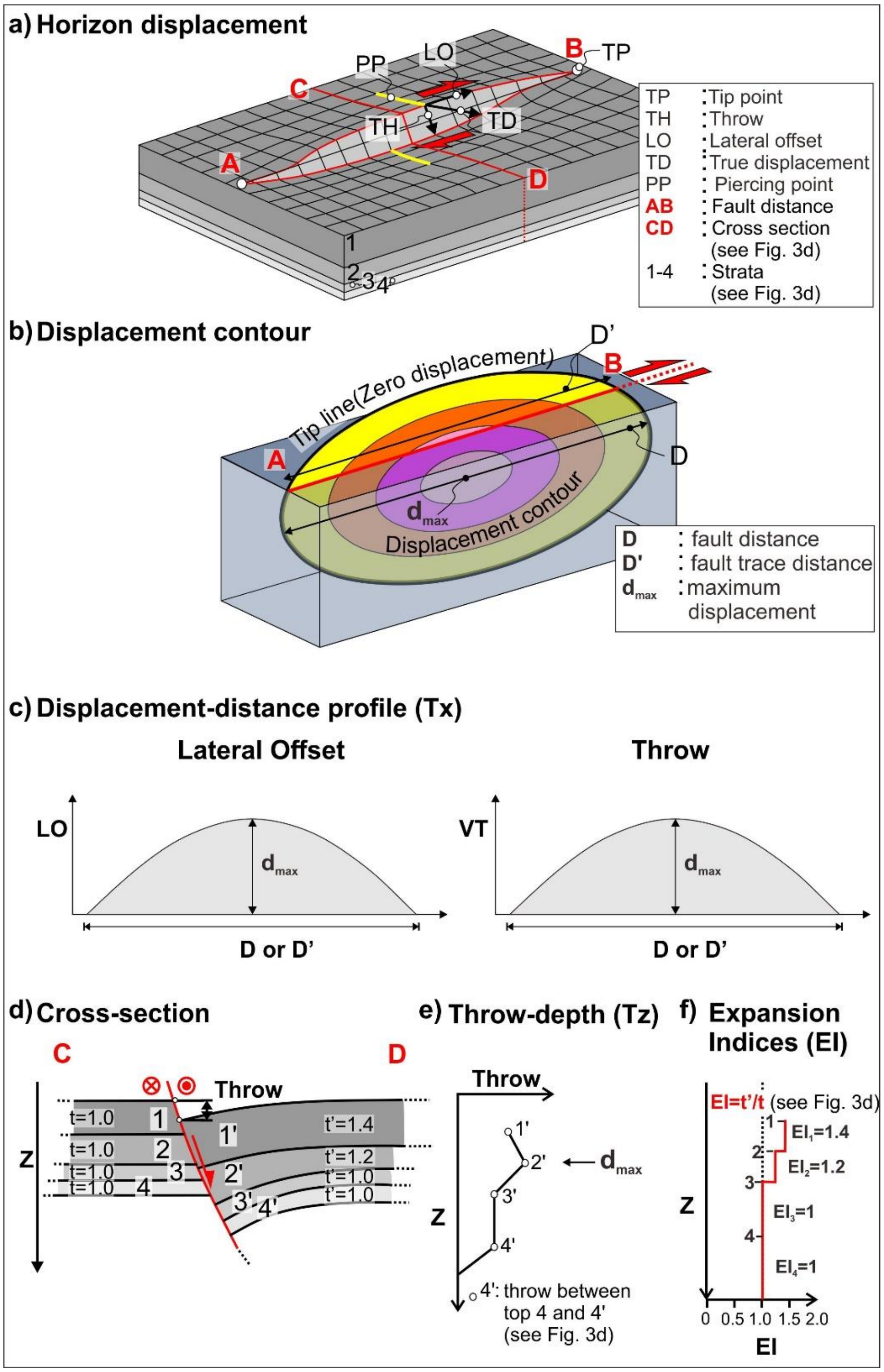

913

Figure 4

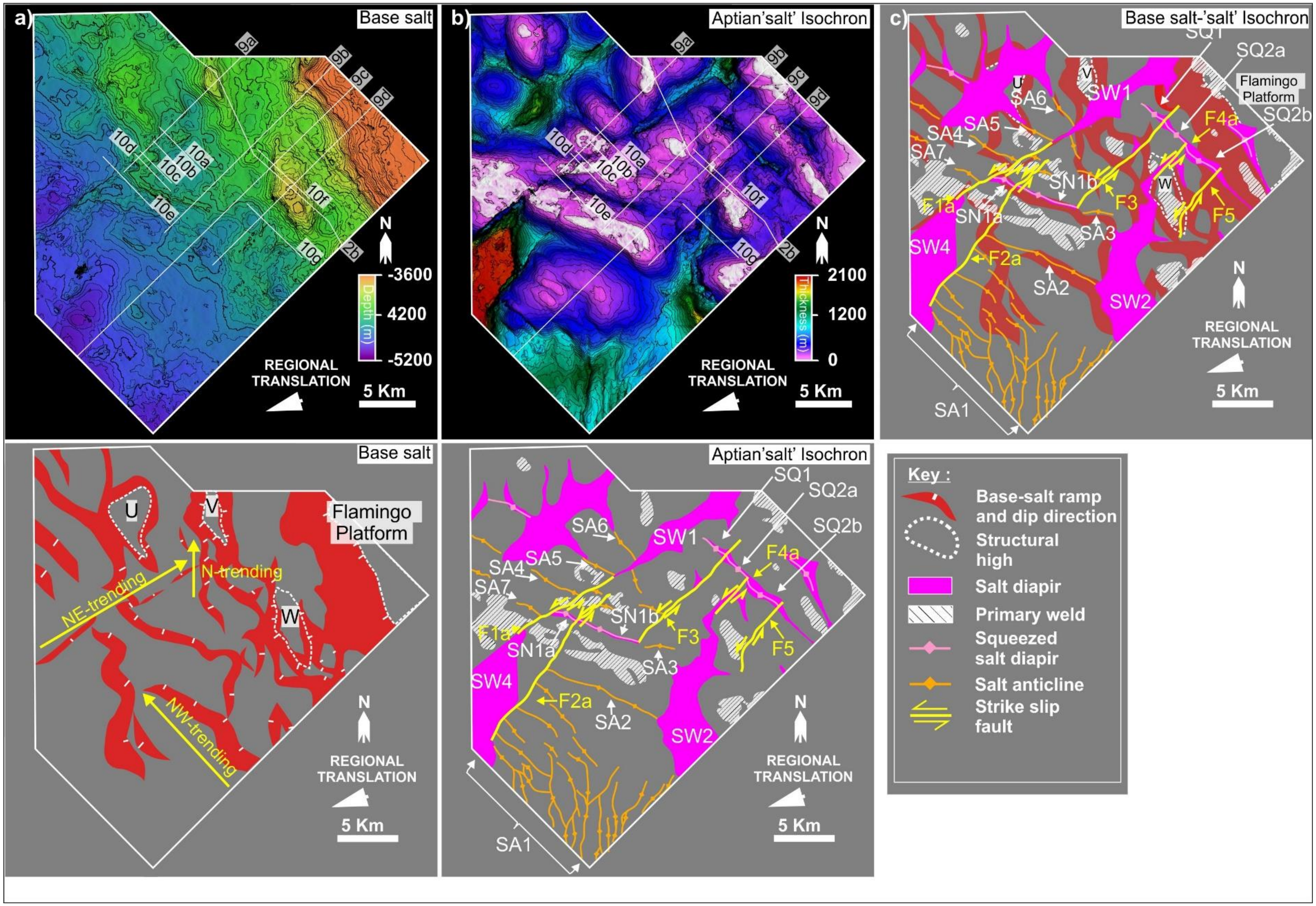

a)
Base salt
9a
9b
9c
9d
10d
10a
10b
10c
10f
10e
10g
2b
N
-3600
4200
-5200
Depth (m)
REGIONAL TRANSLATION
5 Km
b)
Aptian'salt' Isochron
2100
1200
0
Thickness (m)
c)
Base salt-'salt' Isochron
SQ1
SQ2a
SQ2b
Flamingo Platform
U
V
W
SA1
SA2
SA3
SA4
SA5
SA6
SA7
SW1
SW2
SW4
SN1a
SN1b
F1a
F2a
F3
F4a
F5
NE-trending
N-trending
NW-trending
Key :
Base-salt ramp and dip direction
Structural high
Salt diapir
Primary weld
Squeezed salt diapir
Salt anticline
Strike slip fault

Figure 5

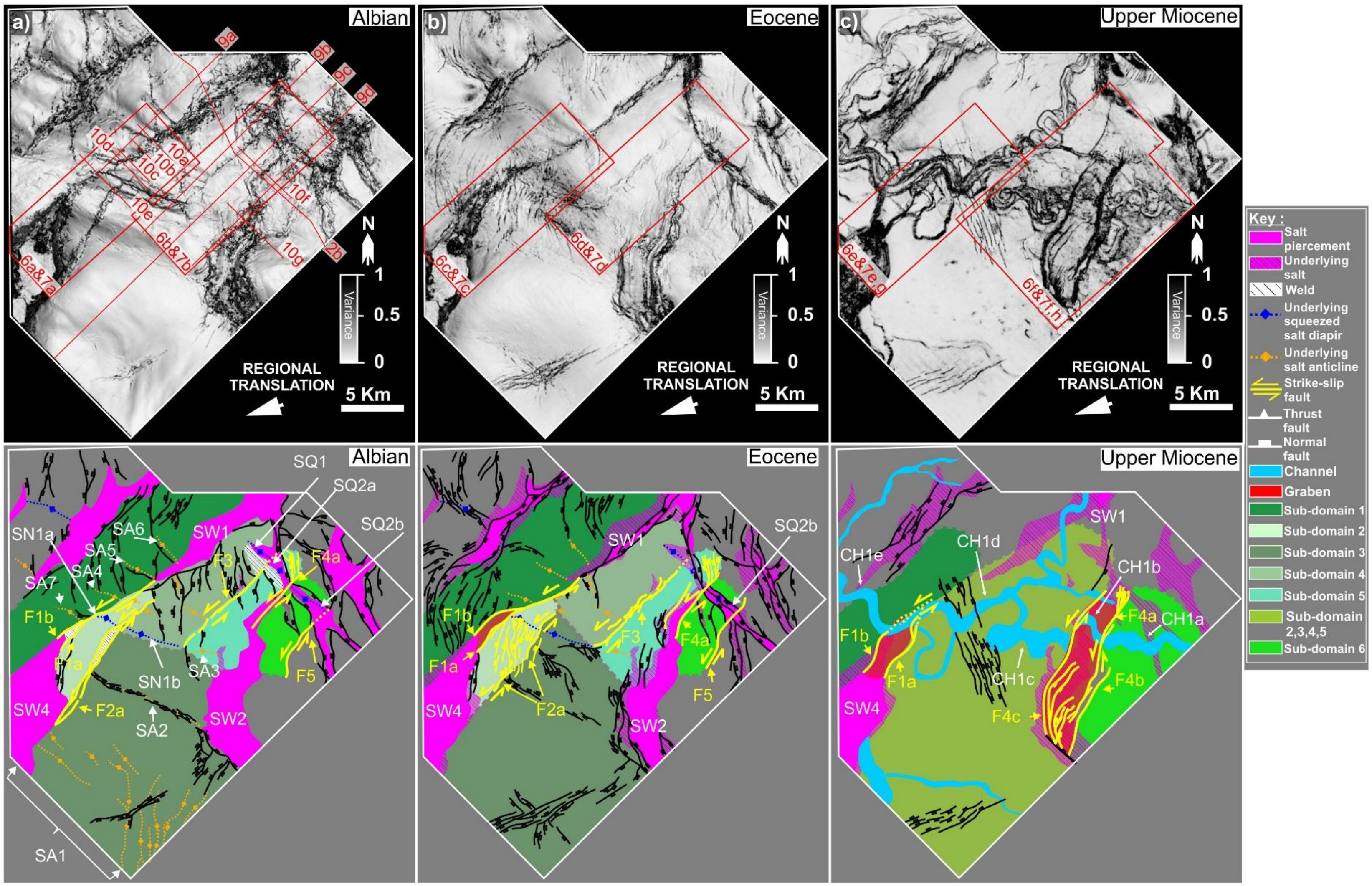

a)
Albian
b)
Eocene
c)
Upper Miocene
REGIONAL TRANSLATION
5 Km
Variance
1
0.5
0
N
Key :
Salt piercement
Underlying salt
Weld
Underlying squeezed salt diapir
Underlying salt anticline
Strike-slip fault
Thrust fault
Normal fault
Channel
Graben
Sub-domain 1
Sub-domain 2
Sub-domain 3
Sub-domain 4
Sub-domain 5
Sub-domain 2,3,4,5
Sub-domain 6

Figure 6

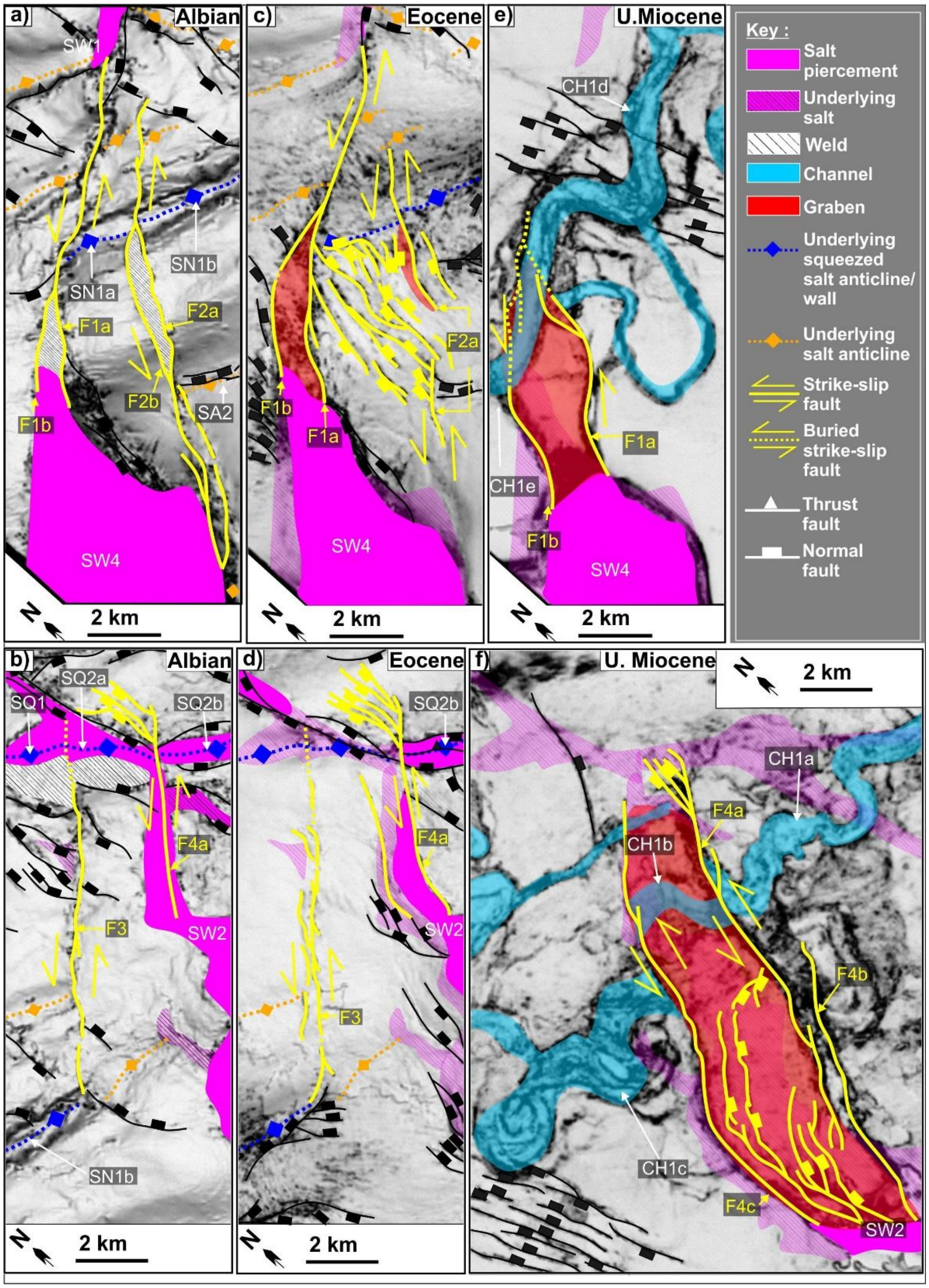
a)
Albian
SW1
SN1a
SN1b
F1a
F2a
F2b
SA2
F1b
SW4
2 km
N
c)
Eocene
F1b
F1a
F2a
SW4
2 km
N
e)
U.Miocene
CH1d
CH1e
F1a
F1b
SW4
2 km
N
Key :
Salt piercement
Underlying salt
Weld
Channel
Graben
Underlying squeezed salt anticline/ wall
Underlying salt anticline
Strike-slip fault
Buried strike-slip fault
Thrust fault
Normal fault
b)
Albian
SQ1
SQ2a
SQ2b
F4a
F3
SW2
SN1b
2 km
N
d)
Eocene
SQ2b
F4a
SW2
F3
2 km
N
f)
U. Miocene
2 km
N
CH1a
F4a
CH1b
F4b
CH1c
F4c
SW2

Figure 7

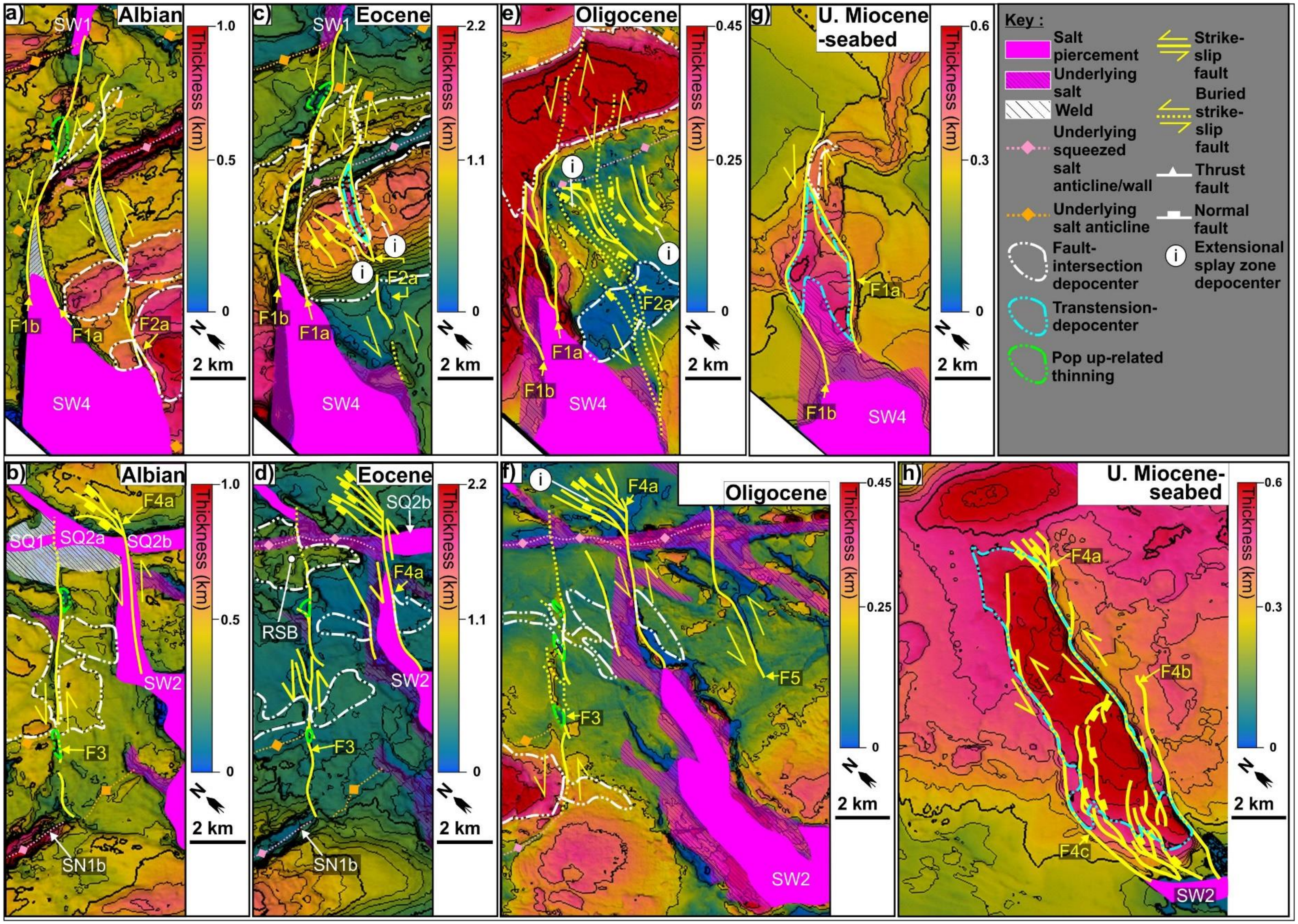

a)
Albian
SW1
F1b
F1a
F2a
SW4
Thickness (km)
1.0
0.5
0
N
2 km
c)
Eocene
SW1
F1b
F1a
F2a
SW4
Thickness (km)
2.2
1.1
0
2 km
e)
Oligocene
F1b
F1a
F2a
SW4
Thickness (km)
0.45
0.25
0
2 km
g)
U. Miocene
-seabed
F1a
F1b
SW4
Thickness (km)
0.6
0.3
0
2 km
Key :
Salt piercement
Underlying salt
Weld
Underlying squeezed salt anticline/wall
Underlying salt anticline
Fault-intersection depocenter
Transtension-depocenter
Pop up-related thinning
Strike-slip fault
Buried strike-slip fault
Thrust fault
Normal fault
Extensional splay zone depocenter
b)
Albian
F4a
SQ1
SQ2a
SQ2b
SW2
F3
SN1b
Thickness (km)
1.0
0.5
0
2 km
d)
Eocene
SQ2b
F4a
RSB
SW2
F3
SN1b
Thickness (km)
2.2
1.1
0
2 km
f)
Oligocene
F4a
F5
F3
SW2
Thickness (km)
0.45
0.25
0
2 km
h)
U. Miocene-
seabed
F4a
F4b
F4c
SW2
Thickness (km)
0.6
0.3
0
2 km

922 Figure 8

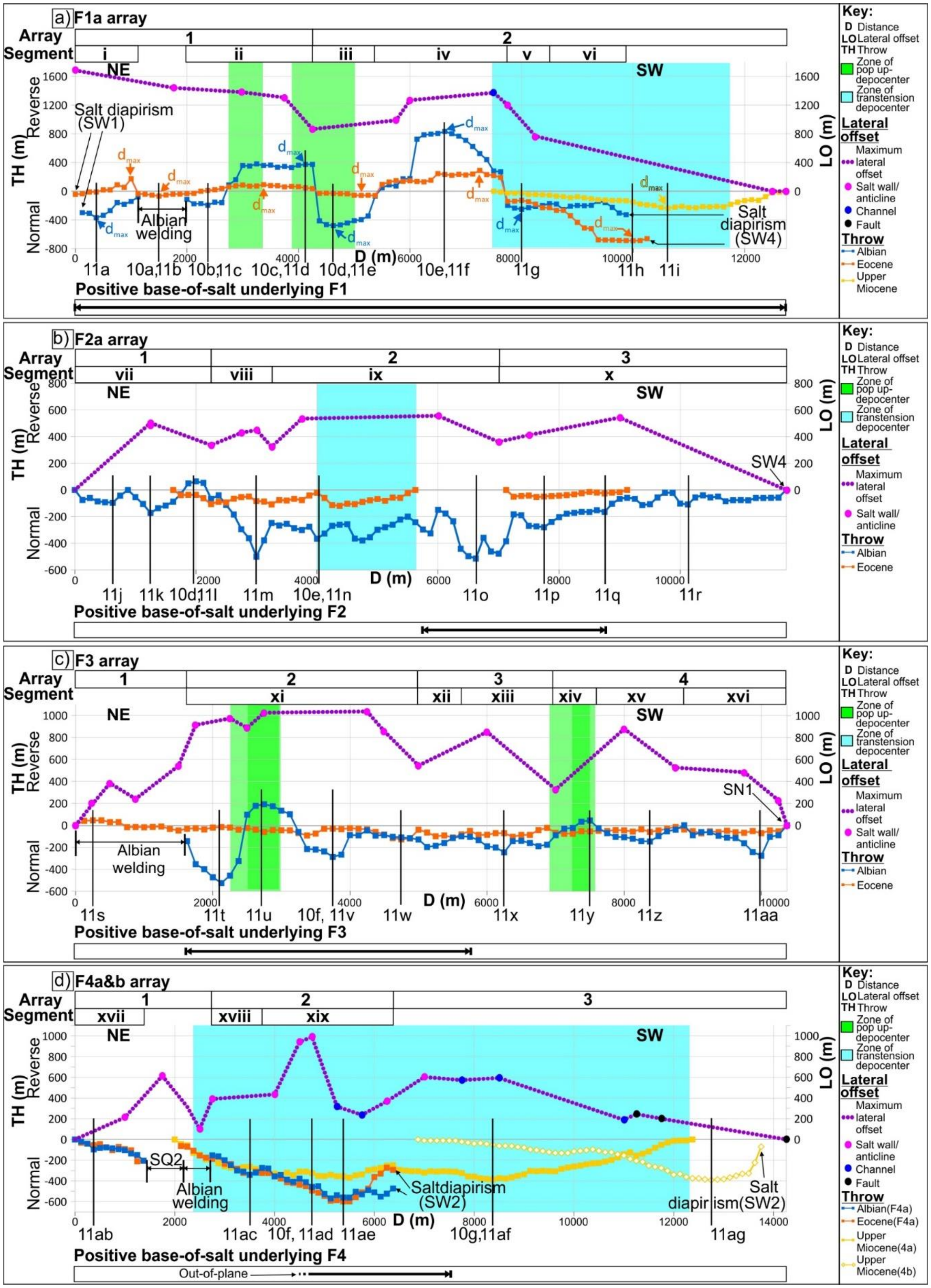

923

Figure 9

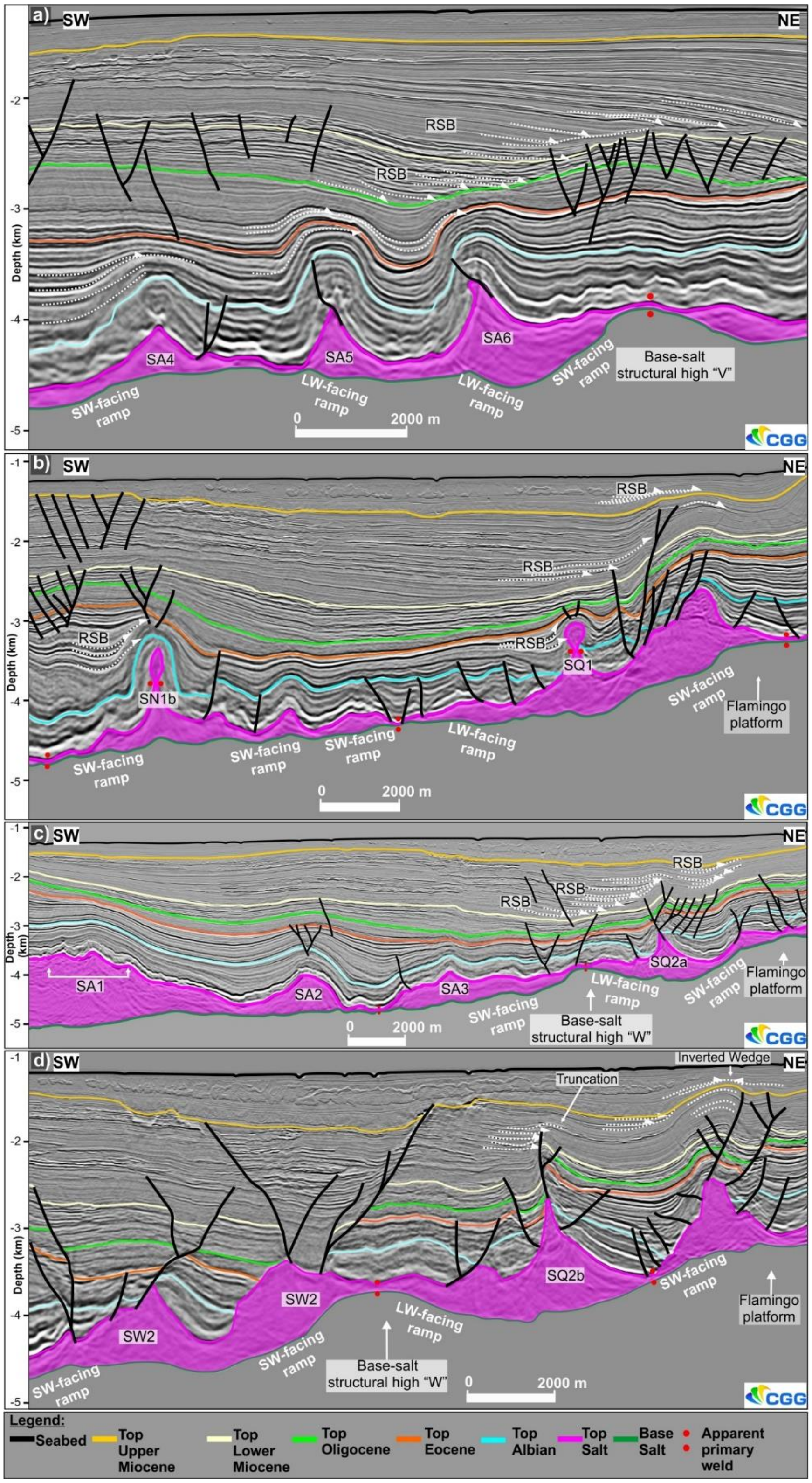
a) SW
NE
Depth (km)
-2
-3
-4
-5
RSB
RSB
SA4
SA5
SA6
SW-facing ramp
LW-facing ramp
LW-facing ramp
SW-facing ramp
Base-salt structural high "V"
0 2000 m
CGG
b) SW
NE
-1
-2
-3
-4
-5
Depth (km)
RSB
RSB
RSB
RSB
SN1b
SQ1
SW-facing ramp
SW-facing ramp
SW-facing ramp
LW-facing ramp
SW-facing ramp
Flamingo platform
0 2000 m
CGG
c) SW
NE
Depth (km)
RSB
RSB
RSB
SA1
SA2
SA3
SQ2a
LW-facing ramp
SW-facing ramp
SW-facing ramp
Flamingo platform
Base-salt structural high "W"
0 2000 m
CGG
d) SW
NE
Inverted Wedge
Truncation
Depth (km)
SW2
SW2
SQ2b
SW-facing ramp
LW-facing ramp
SW-facing ramp
SW-facing ramp
Flamingo platform
Base-salt structural high "W"
0 2000 m
CGG
Legend:
Seabed
Top Upper Miocene
Top Lower Miocene
Top Oligocene
Top Eocene
Top Albian
Top Salt
Base Salt
Apparent primary weld

Figure 10

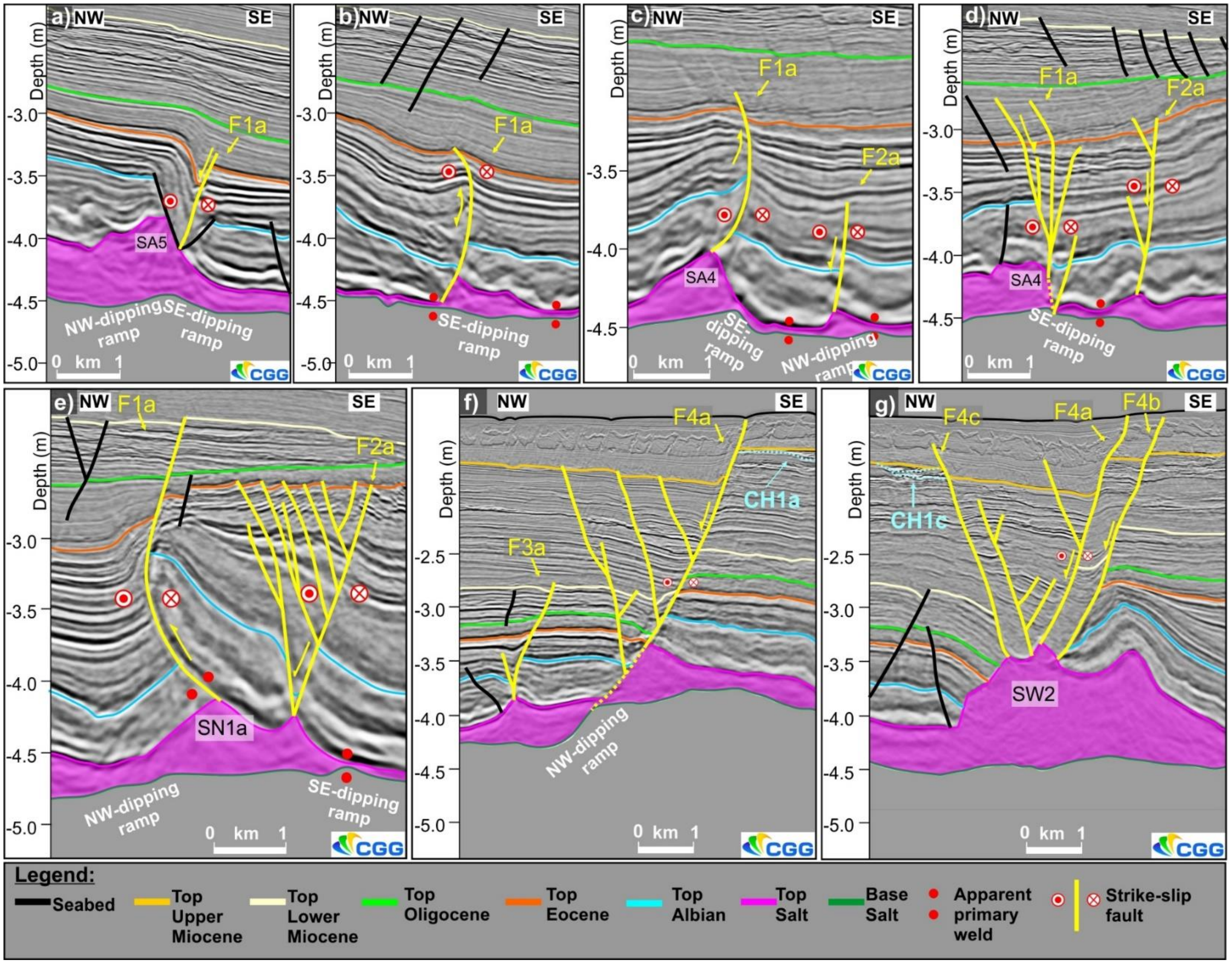

a) NW
SE
Depth (m)
-3.0
-3.5
-4.0
-4.5
-5.0
F1a
SA5
NW-dipping ramp
SE-dipping ramp
0 km 1
CGG
b) NW
SE
F1a
SE-dipping ramp
c) NW
SE
F1a
F2a
SA4
SE-dipping ramp
NW-dipping ramp
d) NW
SE
F1a
F2a
SA4
SE-dipping ramp
e) NW
SE
F1a
F2a
SN1a
NW-dipping ramp
SE-dipping ramp
f) NW
SE
F4a
CH1a
F3a
NW-dipping ramp
g) NW
SE
F4c
F4a
F4b
CH1c
SW2
-2.5
Legend:
Seabed
Top Upper Miocene
Top Lower Miocene
Top Oligocene
Top Eocene
Top Albian
Top Salt
Base Salt
Apparent primary weld
Strike-slip fault

Figure 11

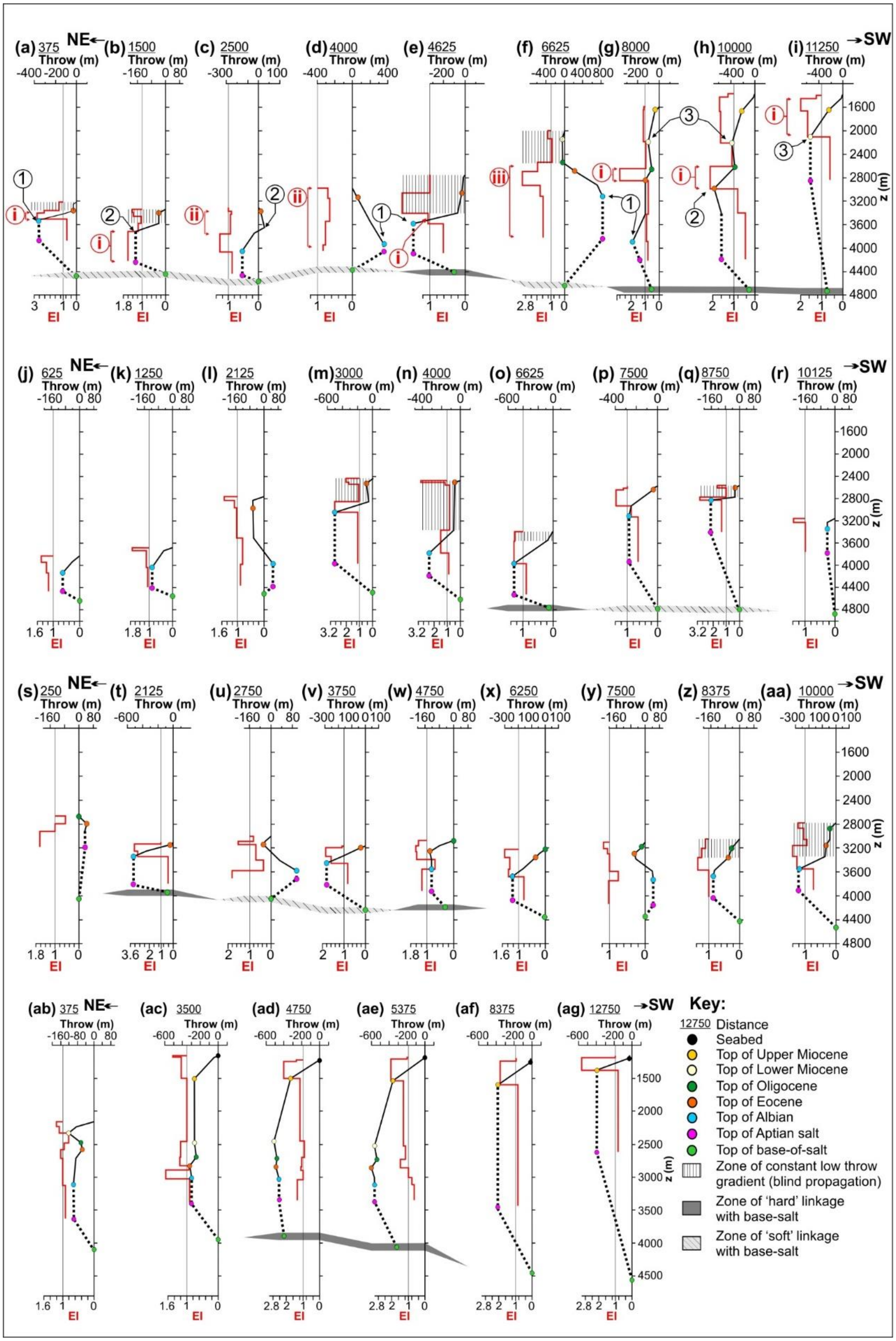

930 Figure 12

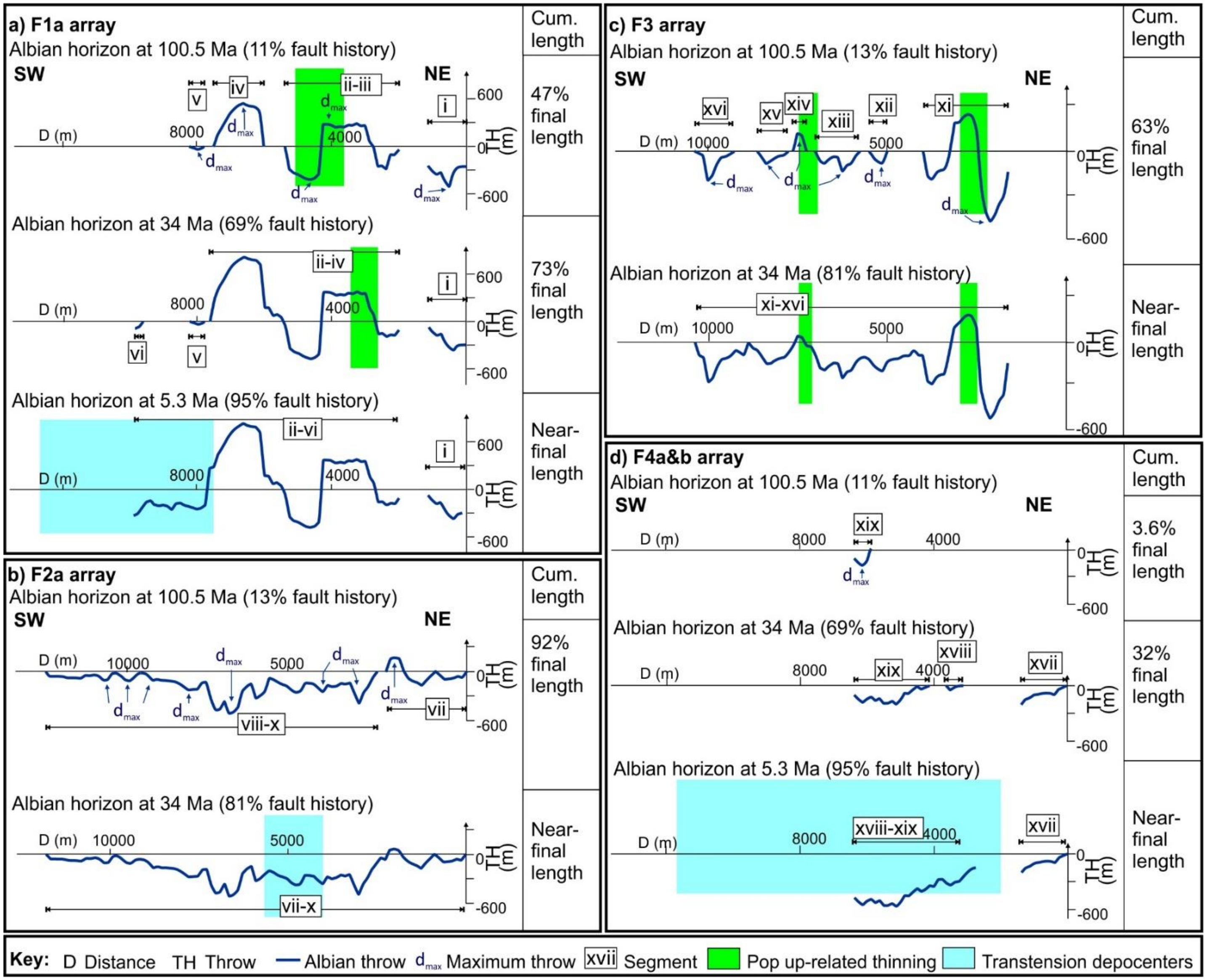

931

932 Figure 13

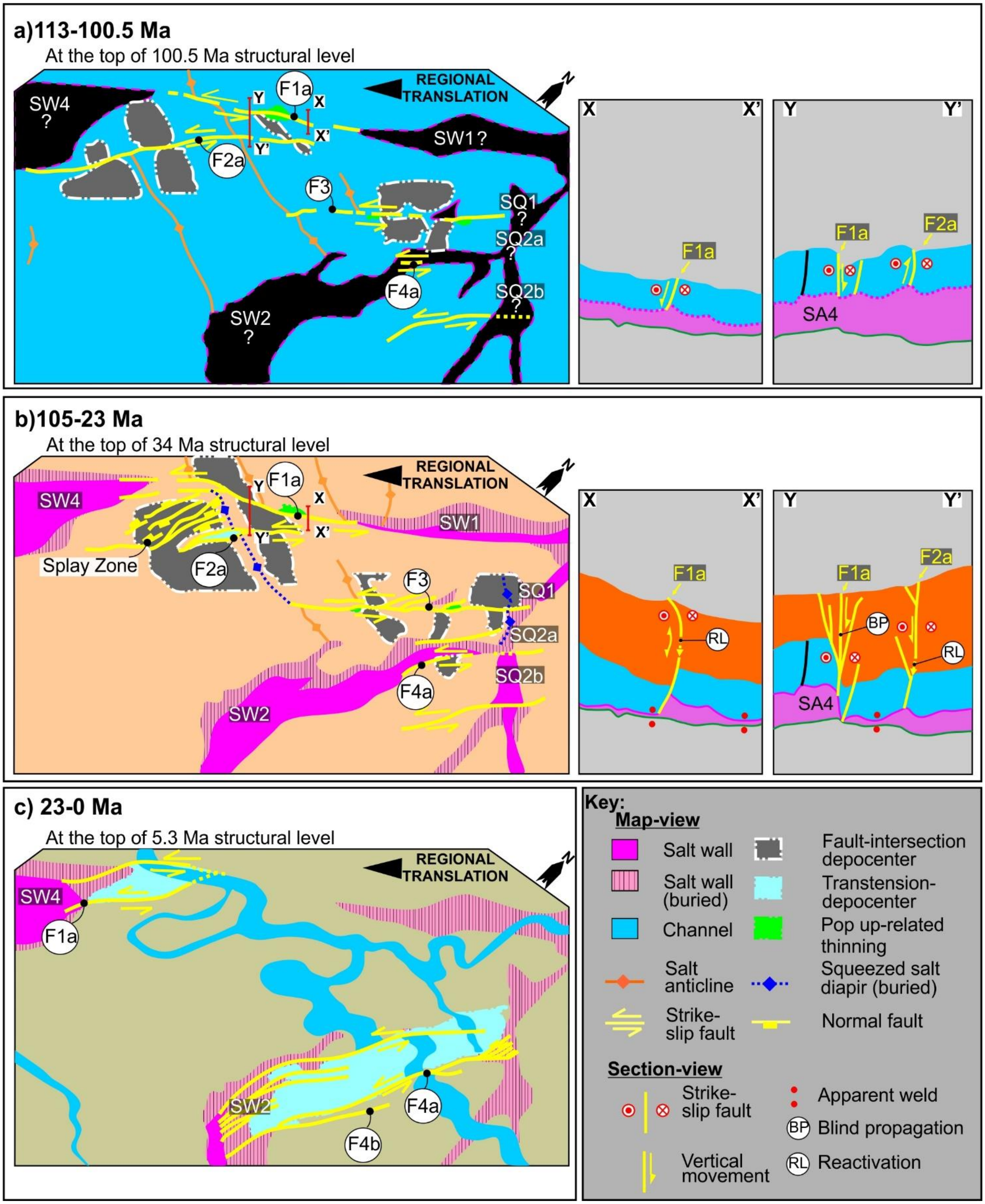

933

934 Figure 14

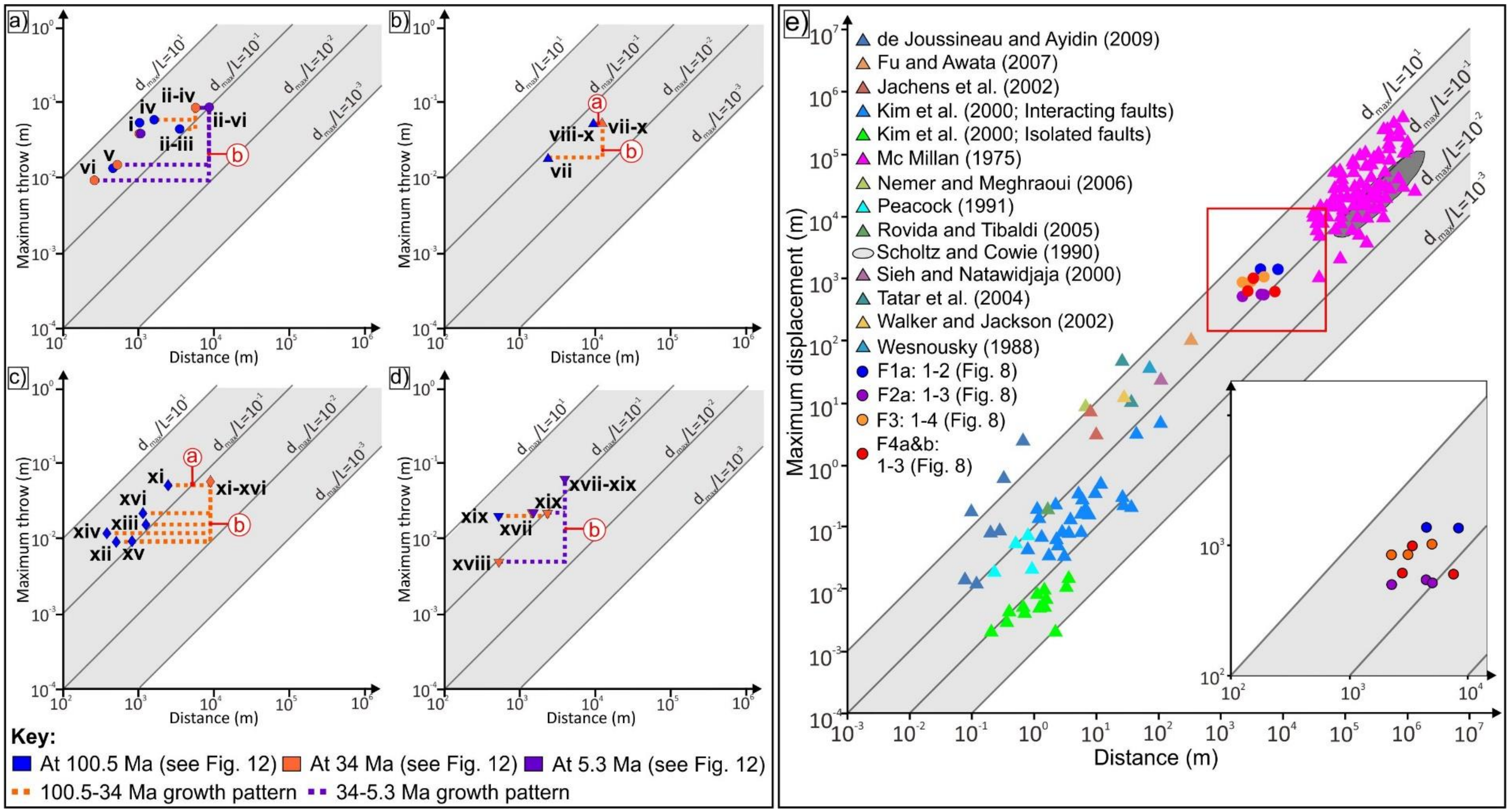

935

Supporting Information for

Salt-detached strike-slip faulting, Outer Kwanza Basin, Offshore Angola

Aurio Erdi[1,2], Christopher A-L. Jackson[1, †]

[1]Basin Research Group (BRG), Department of Earth Science and Engineering, Imperial College, Prince Consort Road, London, SW7 2BP, UK, [2] National Research and Innovation Agency (BRIN), Indonesia, [†] Basin Studies Group, Department of Earth, Atmospheric and Environmental Sciences, University of Manchester, Oxford Road, Manchester, M13 9PL, UK

Contents of this file

Figures S3. Uninterpreted cross sections of Figure 10 across strike-slip faults in the study area (section locations shown in Figures 4a-b and 5a in the main text). Seismic data courtesy of CGG Earth data (previously CGG Multi-Client).

Appendix C. Uninterpreted and interpretative sketch of variance and isopach maps

Figures S4. Uninterpreted zoom in variance map (Figure 6 in main text) at (a-b) Albian, (c-d) Eocene and (e-f) Upper Miocene structural level, documenting variation of map-view geometry of strike-slip faults (map locations shown in Figure 5). Seismic data courtesy of CGG Earth data (previously CGG Multi-Client).

Figure S5. Interpretative sketch map (Figure 6 in main text) of zoom in variance map (Figure S4).

Figure S6. Uninterpreted isopach maps (Figure 7 in main text) of (a-b) Aptian-Albian, (c-d) Albian-Eocene, (e-f) Eocene-Oligocene, (g-h) Upper Miocene to seabed.

Figure S7. Interpretative sketch (Figure 6 in main text) for isopach maps (Figure S6) of (a-b) Aptian-Albian, (c-d) Albian-Eocene, (e-f) Eocene-Oligocene, (g-h) Upper Miocene to seabed.

Appendix D. Data measurements of salt-detached strike-slip faults and collections of global datasets of strike-slip faults

Table S1. Lateral Offset-distance

Table S2. Throw-distance (Tx)

Table S3. Global and our dataset of strike-slip faults

References

Introduction

This supporting information provides: (i) methodological description of fault geometry and kinematic (chapter 3 in main text), (ii) Uninterpreted seismic cross section, (iii) uninterpreted and interpretative sketch of variance and isopach maps, (iv) data measurement of throw and lateral offset of strike-slip fault arrays in the Outer Kwanza Basin (Figure 8 in main text) and collection of global datasets of strike-slip faults (Figures 14c main text).

Appendix A. Methodology of Fault Geometry and Kinematics

We use five techniques to document three-dimensional geometry of and investigate temporal and spatial evolution of salt-detached strike-strike faults above base-salt reliefs, including: i) displacement-distance analysis (Tx); ii) backstripping; iii) fault growth trajectory; iv) vertical separation-depth (c.f. Tz); v) expansion indice (EI); and, vi) isopach map (Fig. S1).

A1. Displacement-distance analysis (Tx)

We conduct displacement-distance analysis (Tx), focusing on the lateral offset of piercing points (i.e. pre-faulting salt structures, channels) (e.g. Peacock, 1991; Kim et al., 2001; 2003; Nixon et al., 2011) *and* the throw of key (seismic) stratigraphic marker horizons (Omosanya et al., 2017; Deng et al., 2019) (Fig. S1a-c). Whereas the density of measurements to constrain lateral offset is dependent on the number of piercing points, the vertical separation is systematically recorded by measuring horizon separation on regularly spaced (125 m) sections oriented perpendicular to the local strike of either master faults or the underlying base-salt relief (see Deng et al., 2019; see also Jackson et al., 2017). We used the throw patterns revealed by our analysis of lateral offset and throw, in particular the presence of strain minima, to detect the positions of linkage between fault segments (e.g. Jackson and Rotevatn, 2013; Tvedt et al., 2016).

A2. Backstripping

We backstrip the throw data to constrain fault kinematics, following similar approach in normal faults (e.g. Jackson et al., 2017). In our study, this method reveals growth in throw accumulation and length of strike-slip faults at times. There are two different backstripping techniques, comprising of: (i) maximum throw subtraction method (Rowan et al., 1998; Dutton and Trudgill, 2009), which honour increasing of fault length as displacement accumulates (e.g. Walsh and Watterson 1988); and, (ii) vertical throw subtraction method (Chapman and Meneilly, 1991; Petersen et al., 1992), which use for a typical fault that has established a near-constant fault length rapidly from an early stage (e.g. Tvedt et al., 2016; Pan et al., 2020). We account for two different reasons that collectively point to the “maximum throw subtraction method’ as a suitable technique for strike-slip faults in the Outer Kwanza Basin. The first reason is that the maximum throw subtraction method, through fault kinematic, promotes fault segments linkage (see Dutton and Trudgill, 2009), a typical geometry and kinematic of strike-slip faults (e.g. Kim and Sanderson, 2005). The second reason is that thickness changes and sediment accumulations across the strike-slip faults and base-salt reliefs do not influence general throw (i.e. vertical component of displacement) distribution; thus, the thickness changed and pre-faulting stratigraphic architecture, as erroneous problems of the maximum throw method, that may influence fault kinematics can be neglected (Jackson, et al., 2017).

A3. Fault growth trajectory

We construct fault growth trajectory using changes in the throw-distance relationships at Albian structural level derived from backstripping (cf. Pan et al., 2022). We choose to only use the Albian structural level due this stratum reflects pre-kinematic stage in Outer Kwanza (Erdi and Jackson, 2021); thus, this stratum records cumulative strain from early- to late- kinematic stages.

A4. Throw-depth (Tz)

We use throw-depth analysis (c.f. T-z) to assess the role of dip linkage in fault growth (Fig. S1d) (e.g. Mansfield and Cartwright, 1995; Cartwright et al., 1998; Tvedt et al., 2016; Jackson and Rotevatn, 2013). The T-z plots were constructed at the location of maximum vertical separation of the Albian and Upper Miocene horizons, whether normal or reverse, on individual segments. Note that, due to seismically imaged of intrasalt stratigraphic horizons, we cannot determine the vertical separation at top salt; we instead assign the nearest separation values of strike-slip faults at the overlying overburden to define them.

A5. Expansion indice (EI)

We construct expansion indices (EI) to investigate thickness variation of growth strata, which reveal temporal activity of the fault kinematics (Fig. S1f) (e.g. Thorsen, 1963; Jackson and Rotevatn, 2013; Reeve et al., 2015; Tvedt et al., 2016).

A6. Isopach map

We make isopach maps to track changes in subsidence and accommodation that mainly relate to the growth of the strike-slip fault array and adjacent salt structures (e.g. Jackson and Rotevatn, 2013; Tvedt et al, 2013).

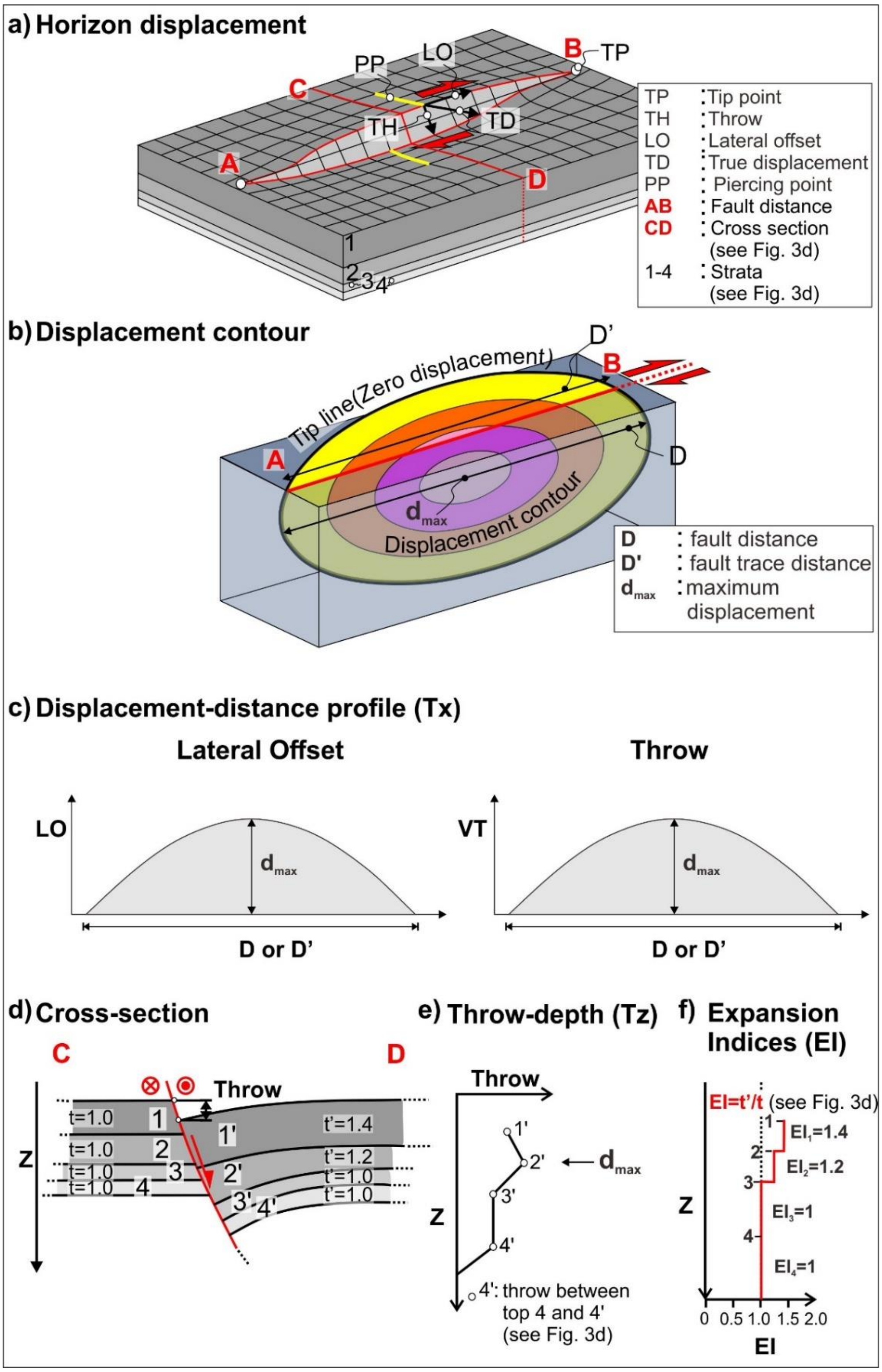

Figure S1. Similar figure with Figure 3 in the main text, illustrating nomenclature and technique to determine geometry of strike-slip faults in this study. (a) oblique view of strike-slip fault; (b) displacement contour on the fault surface; (c) lateral offset and vertical separation displacement profile; (d) hypothetical two-dimensional cross section of a master strike-slip fault; (e) vertical separation-depth; (f) Expansion indices

Appendix B. Uninterpreted seismic cross-section

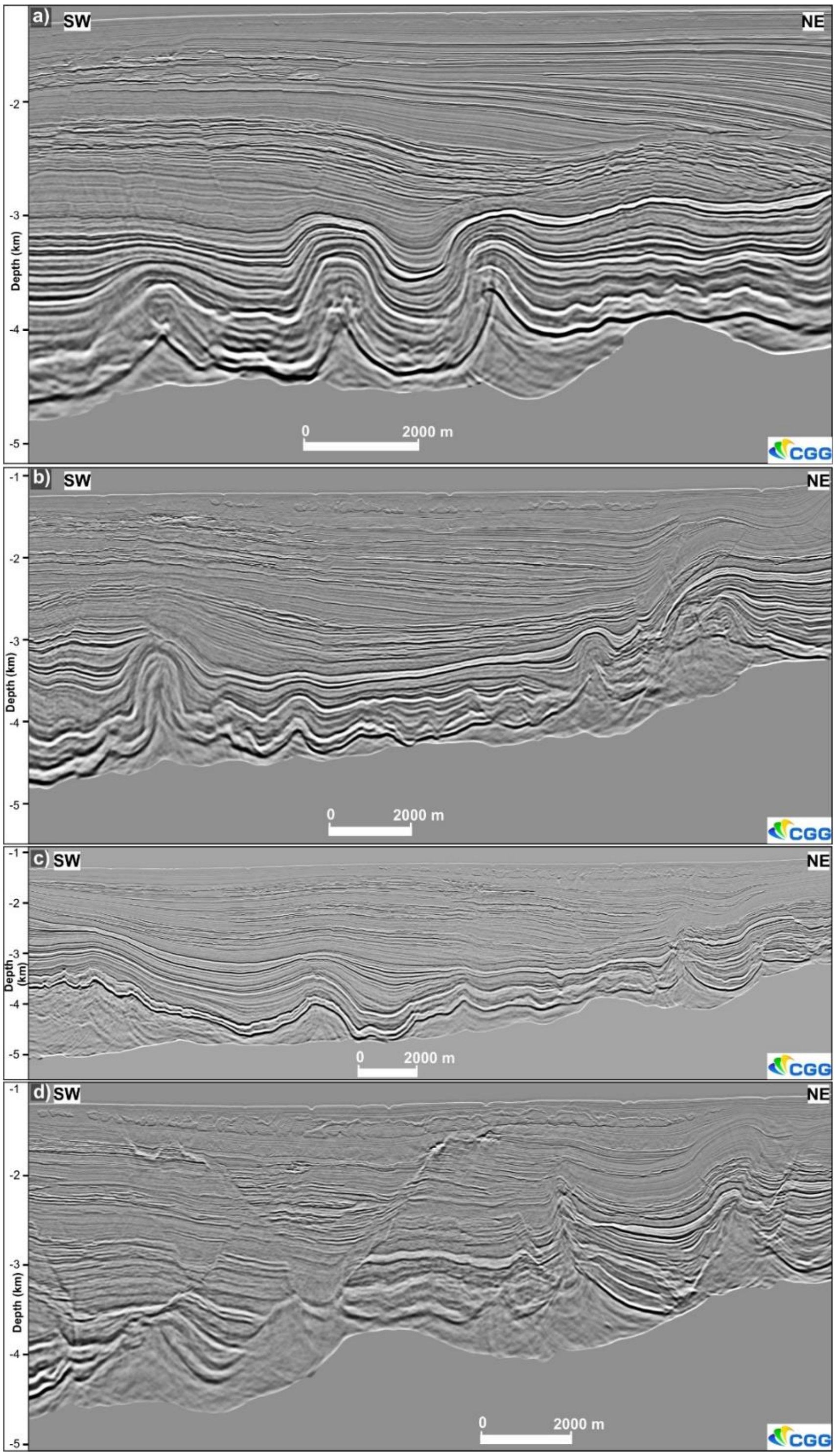

Figure S2. Uninterpreted cross section of Figure 9 that are perpendicular to basin margin and across different domains that are separated by strike-slip faults (section locations shown in Figures 4a-b and 5a in the main text). Seismic data courtesy of CGG Earth data (previously CGG Multi-Client).

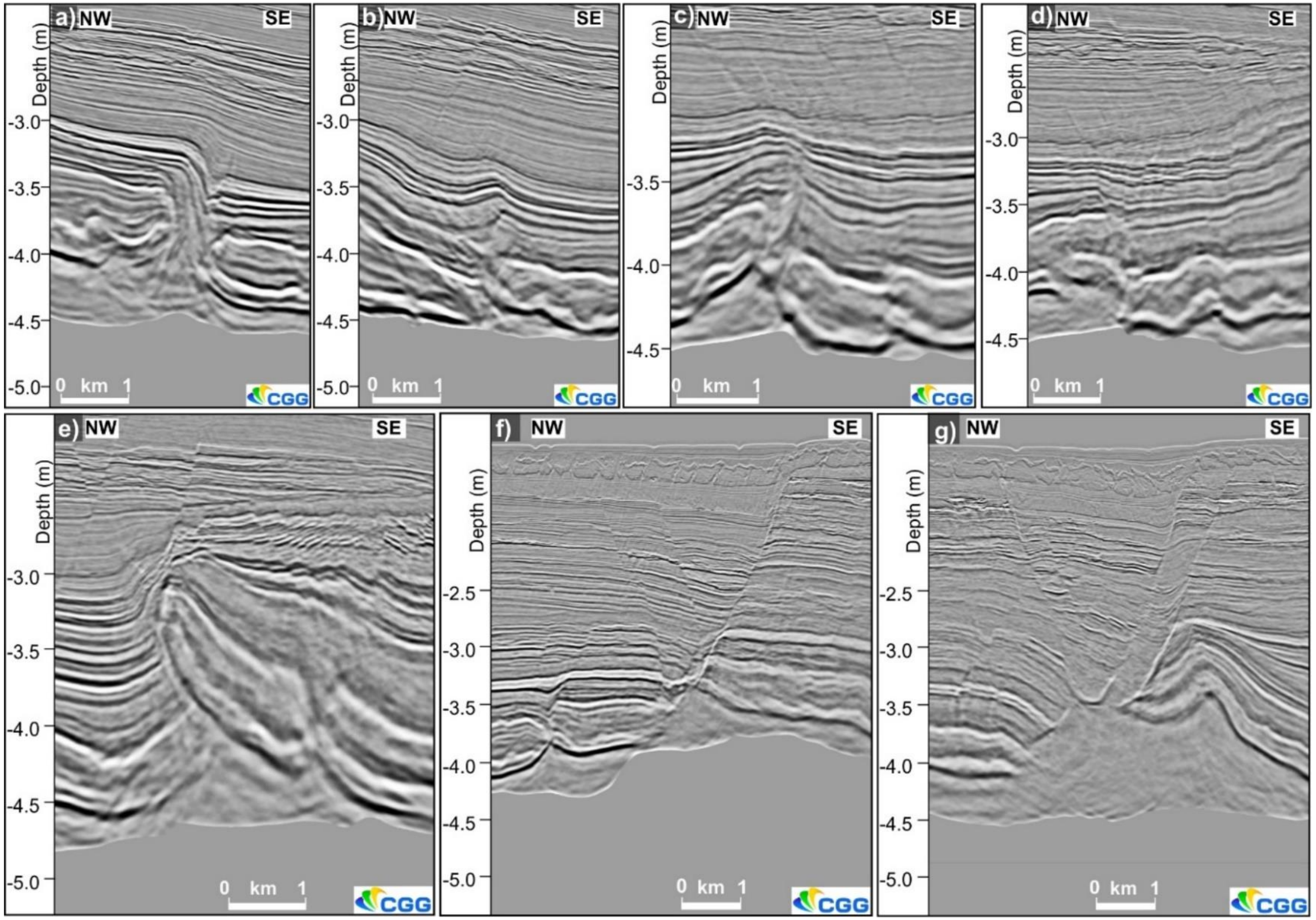

Figure S3. Uninterpreted cross section of Figure 10 across strike-slip faults in the study area (section locations shown in Figures 4a-b and 5a in the main text). Seismic data courtesy of CGG Earth data (previously CGG Multi-Client).

Appendix C. Uninterpreted and interpreted sketch of variance and isopach maps

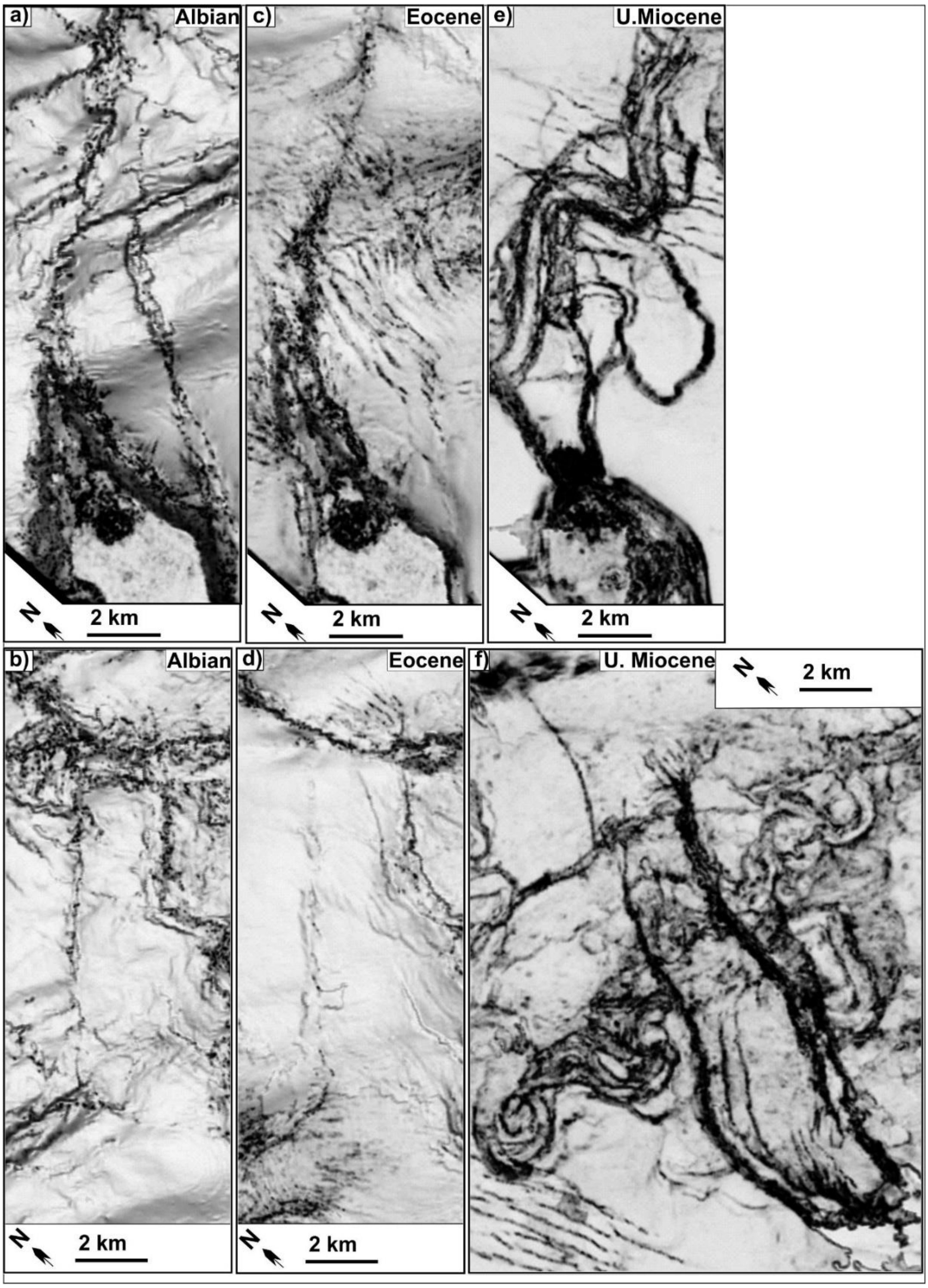

Figure S4. Uninterpreted zoom in variance map (Figure 6 in main text) at (a-b) Albian, (c-d) Eocene and (e-f) Upper Miocene structural level, documenting variation of map-view geometry of strike-slip faults (map locations shown in Figure 5). Seismic data courtesy of CGG Earth data (previously CGG Multi-Client).

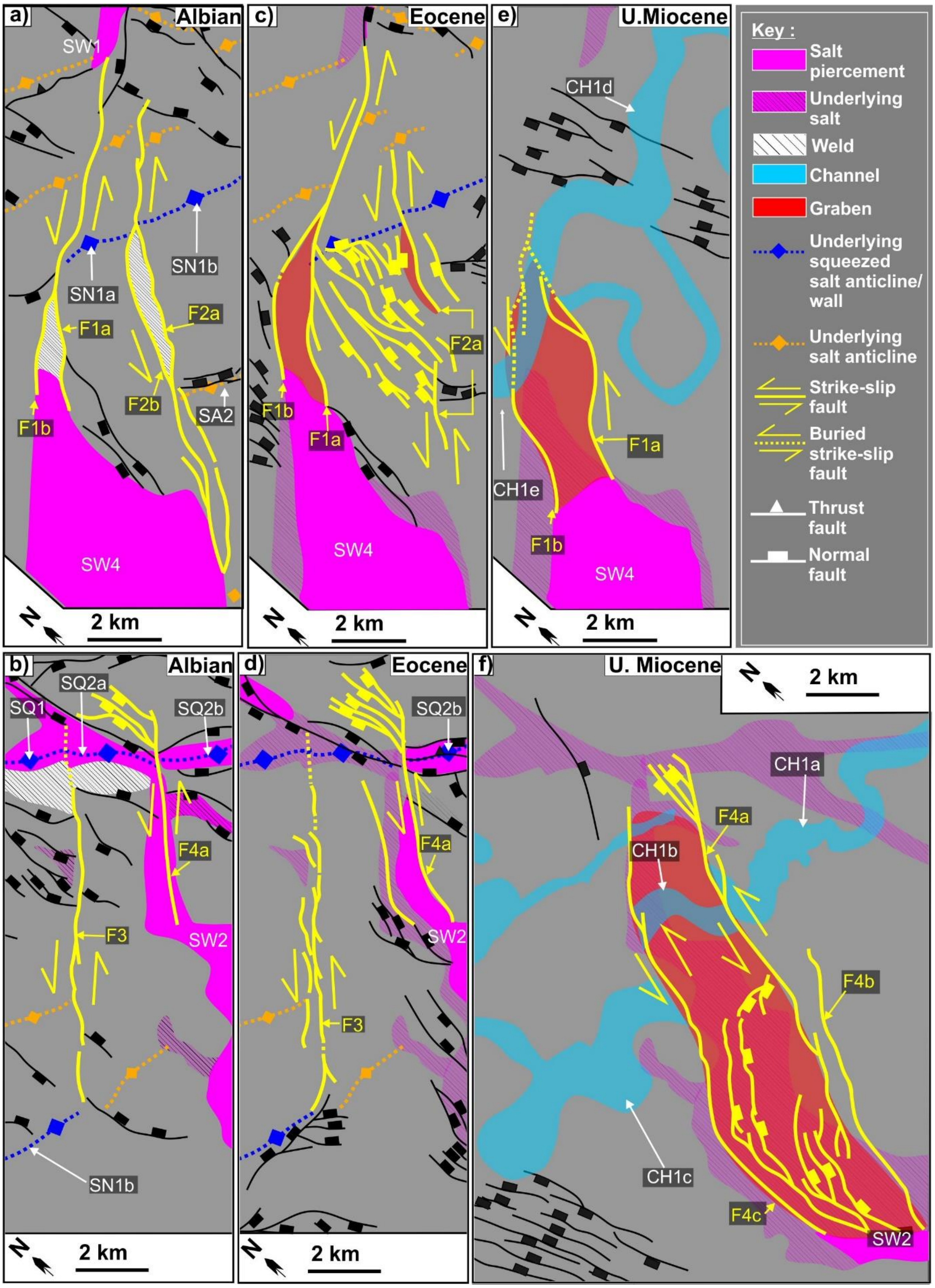

Figure S5. Interpretative sketch map (Figure 6 in main text) of zoom in variance map (Figure S4).

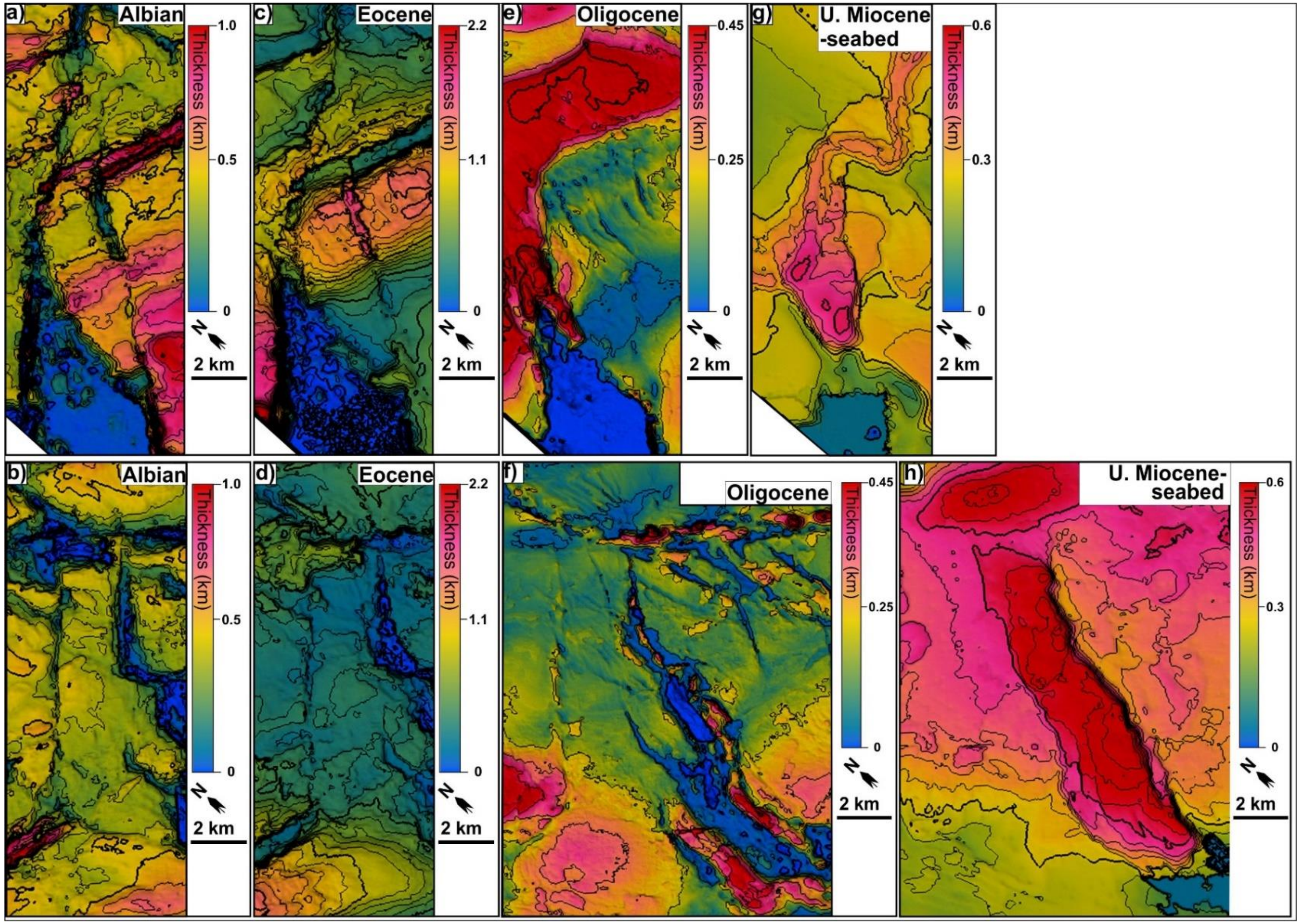

Figure S6. Uninterpreted isopach maps (Figure 7 in main text) of (a-b) Aptian-Albian, (c-d) Albian-Eocene, (e-f) Eocene-Oligocene, (g-h) Upper Miocene to seabed.

1074

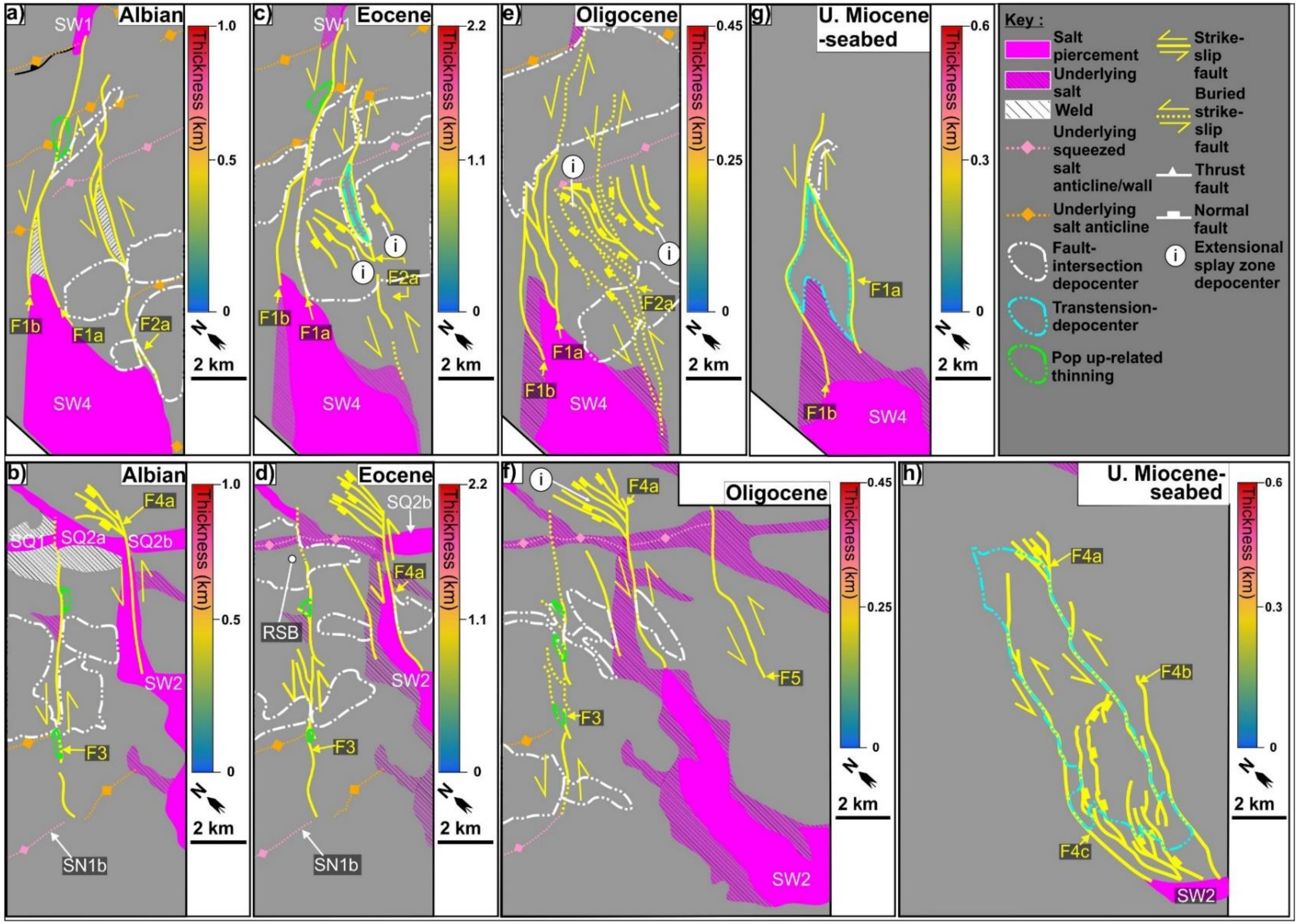

1075 Figure S7. Interpretative sketch (Figure 6 in main text) for isopach maps (Figure S6) of (a-b) Aptian-Albian, (c-d) Albian-Eocene, (e-f) Eocene-Oligocene, (g-h) Upper Miocene to seabed.

Appendix D. Data of salt-detached strike-slip faults and global dataset of strike-slip faults

D1. Lateral Offset-distance

Table S1. Dataset for lateral offset-distance in composite displacement-distance and thickness variation graph (Figure 8 in main article).

<table>
<tr><th colspan="2">F1a</th><th colspan="2">F2a</th><th colspan="2">F3</th><th colspan="2">F4a&b</th></tr>
<tr><th>Distance</th><th>Offset</th><th>Distance</th><th>Offset</th><th>Distance</th><th>Offset</th><th>Distance</th><th>Offset</th></tr>
<tr><td>0</td><td>1683</td><td>0</td><td>0</td><td>0</td><td>0</td><td>0</td><td>0</td></tr>
<tr><td>250</td><td rowspan="6">N/A</td><td>125</td><td rowspan="10">N/A</td><td>125</td><td>N/A</td><td>125</td><td rowspan="7">N/A</td></tr>
<tr><td>500</td><td>250</td><td>250</td><td>198</td><td>250</td></tr>
<tr><td>750</td><td>375</td><td>375</td><td>N/A</td><td>375</td></tr>
<tr><td>1000</td><td>500</td><td>500</td><td>384</td><td>500</td></tr>
<tr><td>1250</td><td>625</td><td>625</td><td rowspan="2">N/A</td><td>625</td></tr>
<tr><td>1500</td><td>750</td><td>750</td><td>750</td></tr>
<tr><td>1750</td><td>1441</td><td>875</td><td>875</td><td>241</td><td>875</td></tr>
<tr><td>2000</td><td rowspan="4">N/A</td><td>1000</td><td>1000</td><td rowspan="4">N/A</td><td>1000</td><td>212</td></tr>
<tr><td>2250</td><td>1125</td><td>1125</td><td>1125</td><td rowspan="5">N/A</td></tr>
<tr><td>2500</td><td>1250</td><td>503</td><td>1250</td><td>1250</td></tr>
<tr><td>2750</td><td>1375</td><td rowspan="6">N/A</td><td>1375</td><td>1375</td></tr>
<tr><td>3000</td><td>1379</td><td>1500</td><td>1500</td><td>543</td><td>1500</td></tr>
<tr><td>3250</td><td rowspan="2">N/A</td><td>1625</td><td>1625</td><td>N/A</td><td>1625</td></tr>
<tr><td>3500</td><td>1750</td><td>1750</td><td>915</td><td>1750</td><td>613</td></tr>
<tr><td>3750</td><td>1305</td><td>1875</td><td>1875</td><td rowspan="3">N/A</td><td>1875</td><td rowspan="3">N/A</td></tr>
<tr><td>4000</td><td>N/A</td><td>2000</td><td>2000</td><td>2000</td></tr>
<tr><td>4250</td><td>865</td><td>2125</td><td>2125</td><td>2125</td></tr>
<tr><td>4500</td><td rowspan="5">N/A</td><td>2250</td><td>336</td><td>2250</td><td>975</td><td>2250</td><td>315</td></tr>
<tr><td>4750</td><td>2375</td><td rowspan="3">N/A</td><td>2375</td><td>N/A</td><td>2375</td><td>N/A</td></tr>
<tr><td>5000</td><td>2500</td><td>2500</td><td>890</td><td>2500</td><td>100</td></tr>
<tr><td>5250</td><td>2625</td><td>2625</td><td>N/A</td><td>2625</td><td>N/A</td></tr>
<tr><td>5500</td><td>2750</td><td>429</td><td>2750</td><td>1027</td><td>2750</td><td>390</td></tr>
<tr><td>5750</td><td>988</td><td>2875</td><td>N/A</td><td>2875</td><td rowspan="4">N/A</td><td>2875</td><td rowspan="4">N/A</td></tr>
<tr><td>6000</td><td>1268</td><td>3000</td><td>450</td><td>3000</td><td>3000</td></tr>
<tr><td>6250</td><td rowspan="2">N/A</td><td>3125</td><td>N/A</td><td>3125</td><td>3125</td></tr>
<tr><td>6500</td><td>3250</td><td>324</td><td>3250</td><td>3250</td></tr>
</table>

6750		3375		3375		3375	
7000		3500	N/A	3500		3500	
7250		3625		3625		3625	
7500	1372	3750	535	3750		3750	
7750	1201	3875		3875		3875	
8000	N/A	4000		4000		4000	434
8250	766	4125		4125		4125	
8500		4250		4250	1038	4250	N/A
8750		4375		4375	N/A	4375	
9000		4500		4500	858	4500	940
9250		4625		4625		4625	N/A
9500		4750		4750	N/A	4750	989
9750		4875	N/A	4875		4875	
10000		5000		5000	545	5000	N/A
10250	N/A	5125		5125		5125	
10500		5250		5250		5250	318
10750		5375		5375		5375	
11000		5500		5500	N/A	5500	N/A
11250		5625		5625		5625	
11500		5750		5750		5750	236
11750		5875		5875		5875	
12000		6000	557	6000	852	6000	N/A
12250		6125		6125		6125	
12500	0	6250		6250		6250	367
12750	N/A	6375		6375		6375	
		6500	N/A	6500	N/A	6500	
		6625		6625		6625	N/A
		6750		6750		6750	
		6875		6875		6875	
		7000	361	7000	327	7000	602
		7125		7125		7125	
		7250	N/A	7250	N/A	7250	N/A
		7375		7375		7375	

[redacted]	7500	412	7500		7500	
	7625		7625		7625	
	7750		7750		7750	572
	7875		7875		7875	
	8000		8000	879	8000	
	8125		8125		8125	N/A
	8250	N/A	8250		8250	
	8375		8375	N/A	8375	
	8500		8500		8500	593
	8625		8625		8625	
	8750		8750	526	8750	
	8875		8875		8875	
	9000	543	9000		9000	
	9125		9125		9125	
	9250		9250	N/A	9250	
	9375		9375		9375	
	9500		9500		9500	
	9625		9625		9625	
	9750		9750	484	9750	N/A
	9875		9875		9875	
	10000		10000	N/A	10000	
	10125		10125		10125	
	10250	N/A	10250	228	10250	
	10375		10375	0	10375	
	10500		[redacted]		10500	
	10625				10625	
	10750				10750	
	10875				10875	
	11000				11000	189
	11125				11125	N/A
	11250				11250	245
	11375				11375	N/A
	11500				11500	

[redacted]	11625		[redacted]	11625	
[redacted]	11750	0	[redacted]	11750	200
[redacted]	[redacted]	[redacted]	[redacted]	11875	
[redacted]	[redacted]	[redacted]	[redacted]	12000	
[redacted]	[redacted]	[redacted]	[redacted]	12125	
[redacted]	[redacted]	[redacted]	[redacted]	12250	
[redacted]	[redacted]	[redacted]	[redacted]	12375	
[redacted]	[redacted]	[redacted]	[redacted]	12500	
[redacted]	[redacted]	[redacted]	[redacted]	12625	
[redacted]	[redacted]	[redacted]	[redacted]	12750	
[redacted]	[redacted]	[redacted]	[redacted]	12875	
[redacted]	[redacted]	[redacted]	[redacted]	13000	N/A
[redacted]	[redacted]	[redacted]	[redacted]	13125	
[redacted]	[redacted]	[redacted]	[redacted]	13250	
[redacted]	[redacted]	[redacted]	[redacted]	13375	
[redacted]	[redacted]	[redacted]	[redacted]	13500	
[redacted]	[redacted]	[redacted]	[redacted]	13625	
[redacted]	[redacted]	[redacted]	[redacted]	13750	
[redacted]	[redacted]	[redacted]	[redacted]	13875	
[redacted]	[redacted]	[redacted]	[redacted]	14000	
[redacted]	[redacted]	[redacted]	[redacted]	14125	
[redacted]	[redacted]	[redacted]	[redacted]	14250	0

D2. Throw-distance (Tx)

Table S2. Dataset for throw-distance in composite displacement-distance and thickness variation graph (Figure 8 in main article).

F1a					F2a				F3				F4a&b					
Distance	Base-salt	Albian	Eocene	Late Miocene	Distance	Base-salt	Albian	Eocene	Distance	Base-salt	Albian	Eocene	Distance	Base-salt	Albian	Eocene	Late Miocene (F4a)	Late Miocene (F4b)
0		-300	-43		0		0		0			0	0		0	0		
125		-300	-37		125		-75		125			41	125		-20	-32		
250		-308	-11		250		-60		250			45	250		-40	-40		
375		-370	-12		375		-85		375			45	375		-97	-54		
500		-337	18		500		-92		500			30	500		-82	-45		
625		-272	18		625		-96		625			30	625		-78	-75		
750		-160	89		750		-43	N/A	750	N/A	Albian welding	-17	750		-85	-103		
875	Present	-183	53	N/A	875	N/A	0		875			-15	875	N/A	-95	-72	N/A	N/A
1000		-142	173		1000		-53		1000			-18	1000		-103	-93		
1125		-80	-35		1125		-105		1125			-14	1125		-136	-105		
1250			-41		1250		-173		1250			-10	1250		-150	-211		
1375			-54		1375		-137		1375			-33	1375		-204	-206		
1500		Albian welding	-68		1500		-117		1500			-47	1500					
1625			-53		1625		-87	0	1625	Present	-144	-31	1625		SQ2			
1750			-42		1750		-32	-38	1750		-354	-27	1750					

1875			-39		1875		49	-36	1875		-400	-37	1875					
2000		-115	-35		2000		64	-36	2000		-473	-20	2000				0	
2125		-177	-30		2125		53	-62	2125		-525	-16	2125		Albian welding	-64	-44	
2250		-173	0		2250		-65	-106	2250		-458	-20	2250			-70	-56	
2375		-194	10		2375		-40	-88	2375		-325	-40	2375			-109	-130	
2500		-153	20		2500		-113	-94	2500		97	-24	2500			-155	-146	
2625		-160	38		2625		-184	-65	2625		178	-40	2625			-176	-192	
2750		88	60		2750		-294	-53	2750		192	-60	2750		-154	-188	-188	
2875		160	74		2875		-362	-49	2875		174	-43	2875		-163	-167	-230	
3000		357	85		3000		-500	-83	3000		134	-45	3000		-200	-235	-260	
3125		351	70		3125		-378	-86	3125		100	-46	3125		-247	-238	-272	
3250		380	72		3250		-247	-109	3250		-61	-70	3250		-300	-282	-294	
3375		357	91		3375		-266	-76	3375		-216	-92	3375		-310	-324	-266	
3500		363	77		3500		-254	-79	3500		-220	-75	3500		-341	-343	-263	
3625		333	76		3625		-287	-66	3625		-237	-31	3625		-320	-310	-284	
3750		345	60		3750		-300	-76	3750		-287	-30	3750		-275	-325	-307	
3875		330	67		3875		-275	-41	3875		-267	-35	3875		-281	-325	-309	
4000		362	63		4000		-366	-20	4000		-89	-26	4000		-357	-354	-328	
4125		373	46		4125		-327	-60	4125		-91	-32	4125		-344	-377	-339	
4250		373	37		4250		-269	-114	4250		-46	-36	4250		-388	-413	-322	
4375		-413	-30		4375		-260	-119	4375		-93	-60	4375		-409	-421	-345	

4500		-465	-27		4500		-257	-103	4500		-89	-84	4500		-379	-437	-310	
4625		-481	-30		4625		-365	-107	4625		-104	-117	4625		-413	-451	-310	
4750		-470	-34		4750		-379	-89	4750		-110	-128	4750		-457	-494	-325	
4875		-444	-37		4875		-355	-78	4875		-117	-120	4875		-451	-514	-351	
5000		-412	-56		5000		-298	-67	5000		-129	-40	5000		-526	-544	-354	
5125		-397	-59		5125		-279	-81	5125		-197	-65	5125		-570	-592	-341	
5250		-346	-57		5250		-260	-57	5250		-186	-100	5250		-538	-586	-355	
5375		-67	-60		5375		-222	-59	5375		-161	-92	5375		-560	-598	-357	
5500		48	94		5500		-200	-23	5500		-116	-111	5500		-561	-598	-368	
5625		88	128		5625		-242	0	5625		-100	-82	5625		-506	-558	-347	
5750		72	146		5750		-296		5750		-105	-51	5750		-530	-510	-338	
5875		171	137		5875		-326		5875		-135	-88	5875	Present	-490	-475	-298	
6000		174	145		6000		-149		6000		-191	-86	6000		-511	-363	-288	
6125		724	136		6125		-177		6125		-202	-72	6125		-552	-329	-274	
6250		786	131		6250		-235		6250		-246	-72	6250		-524	-273	-254	
6375		794	153		6375	Present	-441	N/A	6375	N/A	-144	-104	6375		-473	-293	-248	
6500		804	244		6500		-496		6500		-141	-88	6500				-293	
6625		833	233		6625		-515		6625		-161	-87	6625				-301	
6750		800	222		6750		-359		6750		-190	-43	6750		SW2		-306	
6875		767	235		6875		-461		6875		-176	-23	6875				-306	0
7000		709	226		7000		-477		7000		-90	-68	7000				-320	-10

7125		624	239		7125		-385	0	7125		-30	-76	7125			-307	-10
7250		524	289		7250		-183	-50	7250		-24	-76	7250			-310	-10
7375		440	231		7375		-190	-45	7375		34	-53	7375			-307	-10
7500		281	218	0	7500		-269	-42	7500		44	-55	7500			-309	-10
7625		270	192	-13	7625		-273	-52	7625		-26	-50	7625			-312	-12
7750		-197	-143	-26	7750		-279	-49	7750		-72	-52	7750			-324	-22
7875		-235	-139	-28	7875		-240	-46	7875		-105	-43	7875			-357	-30
8000		-250	-128	-25	8000		-204	-43	8000		-108	-46	8000			-359	-40
8125		-229	-146	-46	8125		-178	-38	8125		-121	-57	8125			-375	-35
8250		-214	-181	-47	8250		-172	-33	8250		-144	-36	8250			-381	-43
8375		-198	-231	-51	8375		-164	-24	8375		-147	-60	8375			-387	-51
8500		-172	-231	-56	8500		-165	-15	8500		-99	-47	8500			-373	-62
8625		-180	-268	-70	8625		-152	-19	8625		-54	-31	8625	N/A		-379	-61
8750		-257	-268	-77	8750		-165	-26	8750		-40	-15	8750			-366	-64
8875		-209	-342	-90	8875		-103	-19	8875		0	-37	8875			-350	-72
9000		-198	-434	-78	9000		-66	-17	9000		-90	-53	9000			-336	-78
9125		-203	-513	-92	9125		-59	0	9125		-62	-73	9125			-304	-97
9250		-196	-522	-105	9250	N/A	-66		9250		-63	-55	9250			-307	-102
9375		-140	-679	-120	9375		-114	N/A	9375		-95	-62	9375			-303	-112
9500		-157	-680	-124	9500		-107		9500		-112	-50	9500			-305	-121
9625		-224	-680	-130	9625		-56		9625		-116	-63	9625			-308	-130

9750		-305	-685	-130	9750		-20		9750		-163	-68	9750			-284	-132
9875		-328	-688	-132	9875		-21		9875		-243	-52	9875			-270	-131
10000			-690	-152	10000		-101		10000		-277	-72	10000			-261	-115
10125			-688	-179	10125		-109		10125		-105	-47	10125			-252	-110
10250			-662	-192	10250		-56		10250		-90	-55	10250			-241	-104
10375				-199	10375		-40		10375		0	0	10375			-231	-96
10500				-227	10500		-55						10500			-227	-110
10625				-239	10625		-49						10625			-213	-123
10750				-222	10750		-84						10750			-198	-123
10875				-212	10875		-77						10875			-173	-143
11000				-228	11000		-76						11000			-143	-155
11125		N/A		-232	11125		-78						11125			-124	-188
11250			N/A	-216	11250		-60						11250			-156	-207
11375				-219	11375		-60						11375			-137	-217
11500				-213	11500		-59						11500			-116	-252
11625				-219	11625		-57						11625			-80	-264
11750				-183	11750		0						11750			-52	-276
11875				-153									11875			-30	-302
12000				-132									12000			-13	-340
12125				-121									12125			-10	-333
12250				-127									12250			-10	-362

12375				-76	[redacted]	12375			0	-375
12500				-22		12500				-376
12625				-16		12625				-385
12750				0		12750				-392
						12875				-387
						13000				-382
						13125			N/A	-367
						13250				-350
						13375				-331
						13500				-327
						13625				-224
						13750				-70

D3 Global and our dataset of strike-slip faults

Table S3. Global and our dataset containing of maximum displacement against fault length for strike-slip faults (Figure 14e in main article).

Reference	Length (Log 10^x)	Maximum displacement (Log 10^x)
Mc Millan (1975)	4.583	2.999
	4.924	3.304
	5.350	3.560
	5.229	3.685
	5.117	3.761
	5.202	3.968
	5.354	3.959
	5.619	3.963
	5.471	4.102
	5.570	4.133
	5.354	4.156
	5.256	4.160
	5.139	4.151
	4.973	4.089
	4.937	3.976
	4.933	3.869
	4.848	3.770
	4.597	3.667
	4.552	3.757
	4.641	3.878
	4.543	3.873
	4.588	3.976
	4.498	3.972

	4.493	4.039
	4.606	4.142
	4.709	4.142
	4.713	3.976
	4.830	4.138
	4.749	4.151
	4.830	4.295
	4.915	4.142
	4.933	4.286
	4.834	4.434
	4.942	4.447
	5.036	4.295
	5.130	4.281
	5.224	4.286
	5.287	4.286
	5.399	4.286
	5.547	4.277
	5.659	4.277
	5.502	4.366
	5.493	4.420
	5.556	4.505
	5.650	4.465
	5.722	4.425
	5.937	4.456
	6.126	4.389
	5.860	4.592
	5.421	4.611
	5.356	4.443
	5.253	4.513
	5.155	4.457
	5.183	4.373

	4.963	4.485
	4.949	4.583
	4.935	4.681
	4.828	4.695
	4.921	4.713
	5.141	4.816
	5.141	4.690
	5.127	4.863
	5.244	4.961
	5.342	4.793
	5.426	4.816
	5.328	5.003
	5.468	4.923
	5.561	4.905
	5.543	4.993
	5.645	4.695
	5.720	4.891
	5.711	5.073
	5.706	5.143
	5.725	5.269
	5.870	5.264
	5.874	5.367
	5.785	5.479
	5.683	5.381
	5.622	5.381
	5.930	5.572
	6.010	5.171
	6.010	5.073
	5.949	5.003
Wesnousky (1988)	1.861	1.543

Peacock (1991)	-0.636	-1.733
	-0.030	-1.684
	-0.292	-1.275
	-0.095	-1.144
Kim et al (2000; Isolated Faults)	0.561	-1.832
	0.523	-1.976
	0.166	-2.020
	0.054	-2.089
	-0.172	-2.295
	0.091	-2.308
	0.173	-2.295
	-0.147	-2.395
	-0.397	-2.370
	-0.435	-2.539
	-0.685	-2.696
	0.348	-2.696
	0.199	-2.170
Kim et al (2000; Interacting fault)	0.081	-0.871
	0.125	-1.172
	-0.100	-1.370
	0.054	-0.723
	0.350	-0.652
	0.718	-0.476
	0.778	-0.570
	0.986	-0.465
	1.074	-0.317
	0.833	-0.718
	0.761	-0.800
	0.586	-0.893
	0.888	-0.811
	0.761	-1.096

	0.454	-1.090
	0.564	-1.107
	0.361	-1.211
	0.389	-1.310
	0.240	-1.468
	0.487	-1.479
	1.442	-0.663
	1.425	-0.531
	1.568	-0.690
	1.647	0.485
	2.035	0.659
Sieh and Natawidjaja (2000)	2.044	1.356
Walker and Jackson (2002)	1.448	1.074
Jachens et al. (2002)	1.001	0.474
	0.908	0.844
Tatar et al. (2004)	1.566	0.996
	1.418	1.657
Rovida and Tibaldi (2005)	-0.727	0.224
Fu and Awata (2006)	2.528	1.995
Nemer and Meghraoui (2006)	0.830	0.926
de Joussineau and Ayidin (2009)	-0.923	-1.923
	-1.110	-1.854
	-0.699	-1.102
	-0.550	-1.068

	-1.007	-0.761
	-0.484	-0.224
	-0.176	0.378
F1a (Our study)	3.641	3.140
	3.923	3.137
F2a (Our study)	3.352	2.702
	3.699	2.728
	3.653	2.735
F3 (Our study)	3.699	3.016
	3.352	2.930
	3.495	2.944
F4a&b (Our study)	3.439	2.787
	3.528	2.995
	3.875	2.780

References

Cartwright, J. A., & Mansfield, C. S. (1998). Lateral displacement variation and lateral tip geometry of normal faults in the Canyonlands National Park, Utah. *Journal of Structural Geology, 20*(1), 3-19. doi:10.1016/s0191-8141(97)00079-5

Chapman, T. J., & Meneilly, A. W. (1991). The displacement patterns associated with a reverse-reactivated, normal growth fault. *Geological Society, London, Special Publications, 56*(1), 183-191. doi:10.1144/gsl.sp.1991.056.01.12

de Joussineau, G., & Aydin, A. (2009). Segmentation along Strike-Slip Faults Revisited. 1575-1594. doi:10.1007/978-3-0346-0138-2_3

Deng, S., Li, H., Zhang, Z., Zhang, J., & Yang, X. (2019). Structural characterization of intracratonic strike-slip faults in the central Tarim Basin. *AAPG Bulletin, 103*(1), 109-137. doi:10.1306/06071817354

Dutton, D. M., & Trudgill, B. D. (2009). Four-dimensional analysis of the Sembo relay system, offshore Angola: Implications for fault growth in salt-detached settings. *AAPG Bulletin, 93*(6), 763-794. doi:10.1306/02230908094

Fu, B., & Awata, Y. (2007). Displacement and timing of left-lateral faulting in the Kunlun Fault Zone, northern Tibet, inferred from geologic and geomorphic features. *Journal of Asian Earth Sciences, 29*(2), 253-265. doi:https://doi.org/10.1016/j.jseaes.2006.03.004

Jachens, R. C., Langenheim, V. E., & Matti, J. C. (2002). Relationship of the 1999 Hector Mine and 1992 Landers Fault Ruptures to Offsets on Neogene Faults and Distribution of Late Cenozoic Basins in the Eastern California Shear Zone. *Bulletin of the Seismological Society of America, 92*(4), 1592-1605. doi:10.1785/0120000915

Jackson, C. A. L., Bell, R. E., Rotevatn, A., & Tvedt, A. B. M. (2017). Techniques to determine the kinematics of synsedimentary normal faults and implications for fault growth models. *Geological Society, London, Special Publications, 439*(1), 187-217. doi:10.1144/sp439.22

Jackson, C. A. L., & Rotevatn, A. (2013). 3D seismic analysis of the structure and evolution of a salt-influenced normal fault zone: A test of competing fault growth models. *Journal of Structural Geology, 54*, 215-234. doi:10.1016/j.jsg.2013.06.012

Kim, Y.-S., Andrews, J. R., & Sanderson, D. J. (2000). Damage zones around strike-slip fault systems and strike-slip fault evolution, Crackington Haven, southwest England. *Geosciences Journal, 4*(2), 53. doi:10.1007/BF02910127

Kim, Y.-S., Andrews, J. R., & Sanderson, D. J. (2001). Reactivated strike–slip faults: examples from north Cornwall, UK. *Tectonophysics, 340*(3-4), 173-194. doi:10.1016/s0040-1951(01)00146-9

Kim, Y.-S., & Sanderson, D. J. (2005). The relationship between displacement and length of faults: a review. *Earth-Science Reviews, 68*(3-4), 317-334. doi:10.1016/j.earscirev.2004.06.003

Mansfield, C. S., & Cartwright, J. (1996). High resolution fault displacement mapping from three-dimensional seismic data: evidence for dip linkage during fault growth.

McMillan, R. A. (1975). *The orientation and sense of displacement of strike–slip faults in continental crust.* (Bachelor). Carleton University, Ottawa, Ontario.

Nemer, T., & Meghraoui, M. (2006). Evidence of coseismic ruptures along the Roum fault (Lebanon): a possible source for the AD 1837 earthquake. *Journal of Structural Geology, 28*(8), 1483-1495. doi:https://doi.org/10.1016/j.jsg.2006.03.038

Nixon, C. W., Sanderson, D. J., & Bull, J. M. (2011). Deformation within a strike-slip fault network at Westward Ho!, Devon U.K.: Domino vs conjugate faulting. *Journal of Structural Geology, 33*(5), 833-843. doi:10.1016/j.jsg.2011.03.009

Omosanya, K. O., Zervas, I., Mattos, N. H., Alves, T. M., Johansen, S. E., & Marfo, G. (2017). Strike-Slip Tectonics in the SW Barents Sea During North Atlantic Rifting (Swaen Graben, Northern Norway). *Tectonics, 36*(11), 2422-2446. doi:10.1002/2017TC004635

Pan, S., Bell, R. E., Jackson, C. A. L., & Naliboff, J. (2022). Evolution of normal fault displacement and length as continental lithosphere stretches. *Basin Research, 34*(1), 121-140. doi:https://doi.org/10.1111/bre.12613

Peacock, D. C. P. (1991). Displacements and segment linkage in strike-slip fault zones. *Journal of Structural Geology, 13*(9), 1025-1035. doi:10.1016/0191-8141(91)90054-m

Petersen, K., Clausen, O. R., & Korstgård, J. A. (1992). Evolution of a salt-related listric growth fault near the d-1 well, block 5605, danish north sea: displacement history and salt kinematics.

Journal of Structural Geology, *14*(5), 565-577. doi:https://doi.org/10.1016/0191-8141(92)90157-R

Reeve, M. T., Bell, R. E., Duffy, O. B., Jackson, C. A. L., & Sansom, E. (2015). The growth of non-colinear normal fault systems; What can we learn from 3D seismic reflection data? *Journal of Structural Geology*, *70*, 141-155. doi:10.1016/j.jsg.2014.11.007

Rovida, A., & Tibaldi, A. (2005). Propagation of strike-slip faults across Holocene volcano-sedimentary deposits, Pasto, Colombia. *Journal of Structural Geology*, *27*(10), 1838-1855. doi:https://doi.org/10.1016/j.jsg.2005.06.009

Rowan, M. G., Hart, B. S., Nelson, S., Flemings, P. B., & Trudgill, B. D. (1998). Three-dimensional geometry and evolution of a salt-related growth-fault array: Eugene Island 330 field, offshore Louisiana, Gulf of Mexico. *Marine and Petroleum Geology, 15*(4), 309-328. doi:10.1016/s0264-8172(98)00021-x

Sieh, K., & Natawidjaja, D. (2000). Neotectonics of the Sumatran fault, Indonesia. *Journal of Geophysical Research: Solid Earth*, *105*(B12), 28295-28326. doi:https://doi.org/10.1029/2000JB900120

Tatar, O., Piper, J. D. A., Gürsoy, H., Heimann, A., & Koçbulut, F. (2004). Neotectonic deformation in the transition zone between the Dead Sea Transform and the East Anatolian Fault Zone, Southern Turkey: a palaeomagnetic study of the Karasu Rift Volcanism. *Tectonophysics, 385*(1), 17-43. doi:https://doi.org/10.1016/j.tecto.2004.04.005

Thorsen, C. E. (1963). Age of growth faulting in south-east Louisiana. *Gulf Costs Association of Geologists Societies Transactions*, *13*, 103-110.

Tvedt, A. B. M., Rotevatn, A., & Jackson, C. A. L. (2016). Supra-salt normal fault growth during the rise and fall of a diapir: Perspectives from 3D seismic reflection data, Norwegian North Sea. *Journal of Structural Geology*, *91*, 1-26. doi:10.1016/j.jsg.2016.08.001

Walker, R., & Jackson, J. (2002). Offset and evolution of the Gowk fault, S.E. Iran: a major intra-continental strike-slip system. *Journal of Structural Geology*, *24*(11), 1677-1698. doi:https://doi.org/10.1016/S0191-8141(01)00170-5

Walsh, J. J., & Watterson, J. (1988). Analysis of the relationship between displacements and dimensions of faults.

Wesnousky, S. G. (1988). Seismological and structural evolution of strike-slip faults. *Nature*, *335*(6188), 340-343. doi:10.1038/335340a0